Lithos 200–201 (2014) 142–156

Contents lists available at ScienceDirect

Lithos

journal homepage: www.elsevier.com/locate/lithos

The geochemical characteristics of Haiyang A-type granite complex in Shandong, eastern China

He Li [a,c], Ming-xing Ling [b], Xing Ding [b], Hong Zhang [c], Cong-ying Li [a], Dun-yi Liu [d], Wei-dong Sun [a,*]

[a] CAS Key Laboratory of Mineralogy and Metallogeny, Guangzhou Institute of Geochemistry, The Chinese Academy of Sciences, Guangzhou 510640, China
[b] State Key Laboratory of Isotope Geochemistry, Guangzhou Institute of Geochemistry, The Chinese Academy of Sciences, Guangzhou 510640, China
[c] State Key Laboratory of Continental Dynamics, Northwest University, Xi'an 710069, China
[d] Beijing SHRIMP Center, Institute of Geology, Chinese Academy of Geological Sciences, 26 Baiwanzhuang Road, Beijing 100037, China

ARTICLE INFO

Article history:
Received 11 December 2013
Accepted 19 April 2014
Available online 2 May 2014

Keywords:
A-type granite
Ridge subduction
North China Craton
Zircon
Oxygen fugacity

ABSTRACT

Haiyang granite complex consists of K-feldspar granite and syenite, with a total exposure area of ~600 km^2. The K-feldspar granite is metaluminous (A/CNK = 0.70 to 0.99) and the syenite is slightly peraluminous (A/CNK = 1.01 to 1.10), both of which have typical characteristics of A-type granite with high total alkali contents and $FeO_T/(FeO_T + MgO)$ ratios. Zircon U–Pb age are 116.8 ± 1.7 Ma and 115.8 ± 2.2 Ma, for the K-feldspar granite and the syenite, respectively. This is consistent with field observation that the syenite intruded into the K-feldspar granite. Varied zircon O isotope (5.65–7.78‰ for K-feldspar granite and 4.68–7.08‰ for syenite) with peak values that are marginally higher than those of mantle zircon reflects important mantle contributions. These together with large variation of zircon $\varepsilon_{Hf}(t)$ values of K-feldspar granite (−22.4 to −15.6) and syenite (−24.6 to −13.5), can best be explained by the involvement of at least two components, e.g., enriched lithospheric mantle +/− subducted materials, and upwelling asthenosphere. Apatite has right decline REE pattern. The apatite from K-feldspar granite has higher Cl contents than those of syenite, implying more influence from a subduction released fluid in K-feldspar granite source. This distinction is supported by the systematically higher oxygen fugacity of K-feldspar granite as indicated by zircon Ce^{4+}/Ce^{3+} ratios. In the Yb/Ta–Y/Nb, Ce/Nb–Y/Nb diagrams, both K-feldspar granite and syenite plot in A_1-type, with K-feldspar granite plotting closer to A_2. In the Nb–Y–3Ga and Nb–Y–Ce charts, syenite plots near the boundary between A_1 and A_2, whereas some K-feldspar granite samples plot in A_2 field, indicating a tendency of transition originally from A_2 to A_1. In general A_1 granites form in intraplate settings, whereas A_2 granite forms in post-collision. It is likely that mantle components metasomatized by subduction released fluids are easier to be partially melted, forming K-feldspar granite (closer to A_2 type) with higher oxygen fugacity, which consequently eliminated subduction signatures, and then followed by A_1 type syenite. Similar to the Lower Yangtze River belt, where both A_1 and A_2 group granites of similar ages outcropped in the same region, Haiyang granite complex may also be plausibly explained by a ridge subduction model, which has been proposed as the mechanism that controlled the decratonization of the North China Craton.

1. Introduction

Shandong Peninsula, as one part of both the North China Craton (NCC) and the Sulu ultrahigh-pressure belt, has received wide attentions. Many studies on this region have been done to understand the destruction of the North China Craton, the oldest tectonic unit in China (Liu et al., 1992), and Mesozoic geodynamic mechanism in eastern China (Chen, 2010; Gao et al., 2004; Liu et al., 2010; Wu et al., 2006; Xu, 2001; Xu et al., 2004; Yang et al., 2003; Zhang et al., 2002; Zhao et al., 2013; Zhu et al., 2012). Given that the continental lithospheric mantle beneath the NCC was dramatically thinned during the Early Cretaceous till Early Tertiary (Xu, 2001; Xu et al., 2004, 2012), Early Cretaceous intrusion rocks, especially A-type granites, are important in revealing the geodynamic mechanism. A-type granites form in extensional environments (Loiselle and Wones, 1979; Whalen et al., 1987). Previous studies on Cretaceous A-type granites in the Lower Yangtze River (LYR) belt in eastern China showed that A_1 and A_2 type granites distributing alternately in three belts, which was explained by the subduction of a ridge between the Pacific and the Izanagi plates in the Early Cretaceous (Li et al., 2012b; Ling et al., 2009; Sun et al., 2010). Shandong Peninsula is located more than 500 km to the north of the LYR belt. Cretaceous A-type granites were also outcropped in this region. A ridge subduction model has been proposed to explain the distribution of adakite and the destruction of the NCC (Ling et al., 2013; Sun et al., 2010).

* Corresponding author. Tel.: +86 20 85290215; fax: +86 20 85290130.
E-mail address: weidongsun@gig.ac.cn (W. Sun).

http://dx.doi.org/10.1016/j.lithos.2014.04.014
0024-4937/

In this contribution, we report geochemical compositions, zircon ages and Hf, O isotopes, and zircon, apatite trace elements of Haiyang granite complex (Figs. 1, 2), aiming to better understand the genesis of these granites and the geodynamic settings in the Early Cretaceous.

2. Geological setting

Shandong Peninsula is located at the southeastern margin of the NCC. It is known as the eastern part of the Dabie–Sulu ultrahigh pressure metamorphic belt that formed by the Triassic collision between the North China and the Yangtze blocks (Goss et al., 2010; Li et al., 1993; Sun et al., 2002; Wang et al., 1995; Xu, 2006; Yang et al., 2005; Zhang, 2012; Zhang et al., 2010; Zheng et al., 2005, 2006). The well-known translithospheric, sinistral Tan–Lu (Tancheng–Lujiang) fault separates the Shandong Peninsula into two segments, Luxi segment in the west and Jiaodong segment in the east (Goss et al., 2010; Li et al., 1993; Tan et al., 2012; Ying et al., 2006; Zhang et al., 2010). Three main periods of Mesozoic magmatism have been reported in the region, i.e., Triassic (Indosinian), Jurassic (Early Yanshanian) and Cretaceous (Late Yanshanian). There is an Early Cretaceous A-type granite belt distributed NEE ward along the whole Shandong Peninsula (Wang et al., 1995, 2009), which is closely associated with the slightly older (~130 Ma) adakite belt (Ling et al., 2013; Zhang et al., 2001) (Fig. 1). From Taolin in Jiangsu province, towards NEE, to Rizhao, Jiaonan, Qingdao, Laoshan, Haiyang, Rushan and Weihai in Shandong province, this A-type granite belt is about 500 km long (Wang et al., 1995). K-feldspar granites followed by alkaline granites were outcropped in the belt as granite complexes (Wang et al., 1995). In addition, there are some Early Cretaceous intrusive and extrusive rocks as well as numerous Early Cretaceous mafic dykes (Zhang and Sun, 2002) formed at 130–110 Ma in the Shandong Peninsula (Fan et al., 2001; Ying et al., 2006).

The Haiyang A-type granite complex is located to the north of Haiyang City (Fig. 2A) with a total outcrop area of ~600 km^2. It intruded into Cretaceous sedimentary rocks, with several small granite mountains known as Zhaohushan, Pingdingshan, Qiguding, Longwangshan and Yuhuangshan. We collected samples from the south part of Longwangshan, which is situated between Haiyang–Qingdao fault and Zhuwu–Dianji fault, containing medium coarse grained K-feldspar granite, fine grained syenite and some mafic dykes (Fig. 2B). In the sample location, the syenite and mafic dykes intruded into the K-feldspar granite, some mafic dyke rocks contain K-feldspar granite xenoliths of up to 8 cm long. The K-feldspar granite mainly consists of medium coarse grained K-feldspar and quartz, with some amphibole and biotite (Fig. 2C). The syenite mainly contains fine grained K-feldspar and quartz (Fig. 2D).

3. Analytical methods

3.1. Whole-rock major and trace element analyses

The major and trace elements of the bulk rock samples were analyzed at the State Key Laboratory of Isotope Geochemistry, Guangzhou Institute of Geochemistry, Chinese Academy of Sciences. The bulk rock major elements were conducted using X-ray fluorescence spectrometry (Rigaku 100e) with analytical precisions better than 1% (Li et al., 2005) and the trace element analysis was carried out on fused glass by using

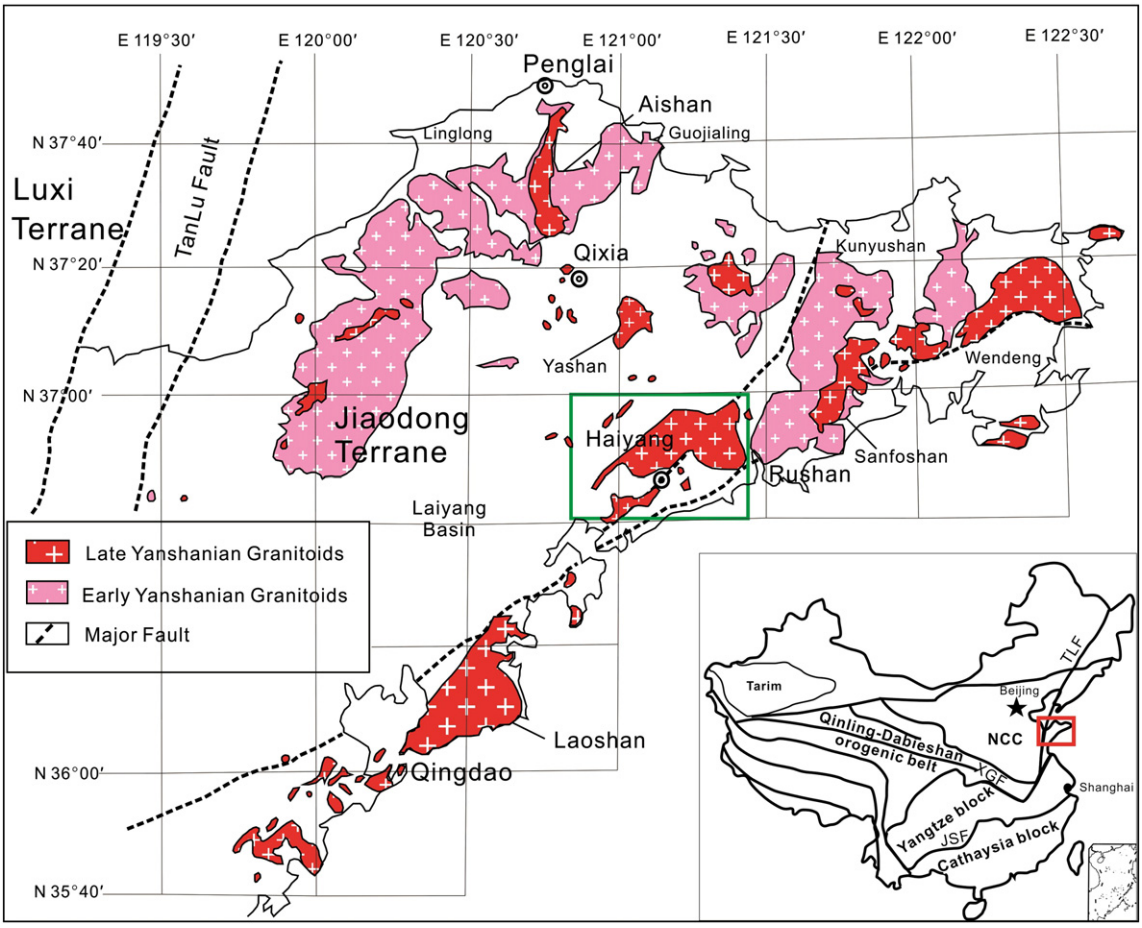

Fig. 1. Simplified geological map of the Shandong Peninsula, showing the distribution of Early Yanshanian and Late Yanshanian granitoids of the Jiaodong Terrane (modified from Goss et al., 2010). Shandong Peninsular located at southeastern part of the NCC. It is also the east part of Sulu UHP metamorphic belt. Tan–Lu fault separates it into two segments, Luxi segment in the west and Jiaodong segment in the east. The rectangle in the map marks the locations of samples and the more detailed map presented in Fig. 2.

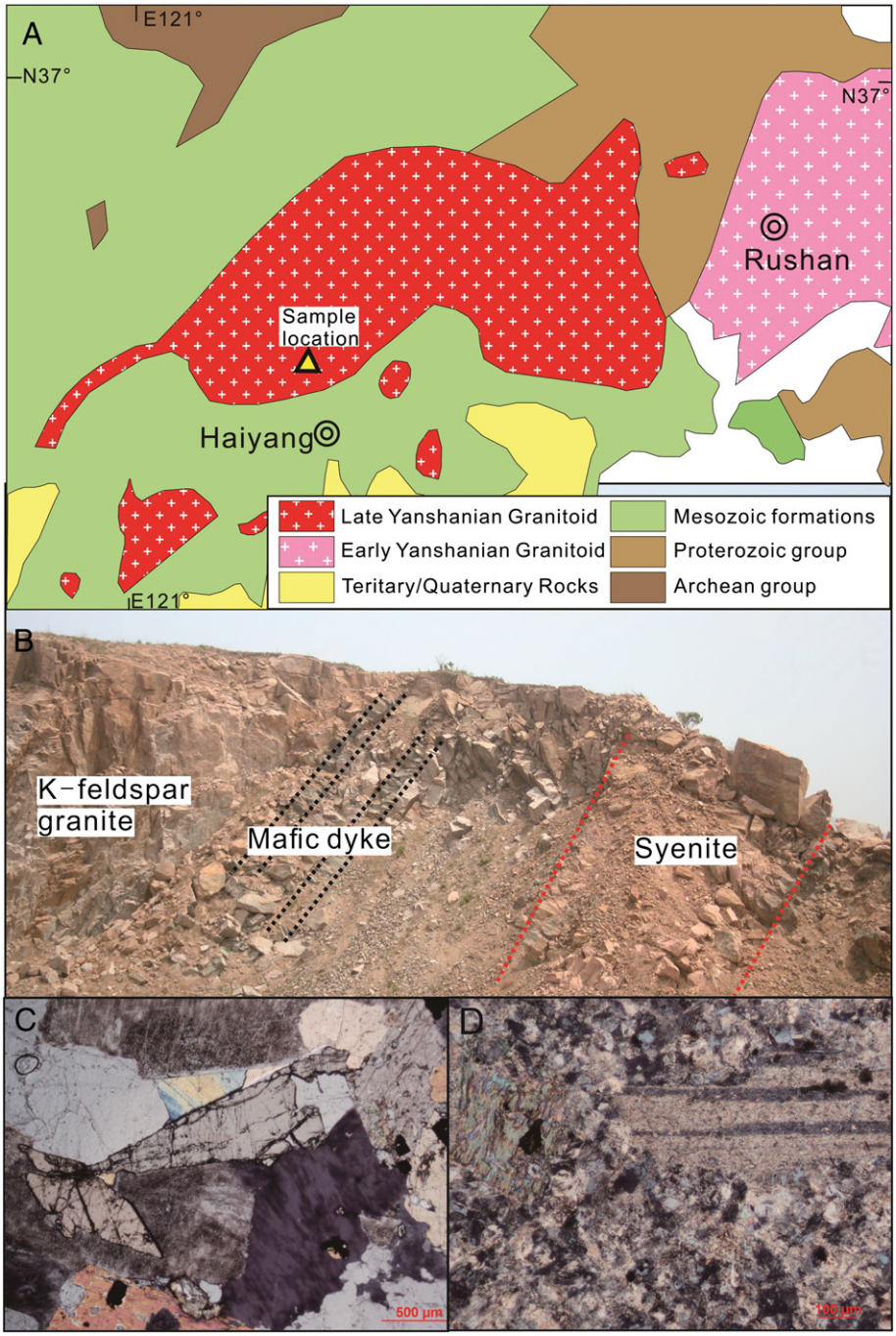

Fig. 2. A. Geological map of the Haiyang granite complex showing sample location. It is located to the north of Haiyang City and contains K-feldspar granite and syenite with some mafic dykes. B. Picture of Haiyang pluton, showing the syenite and the mafic dykes intruded into the K-feldspar granite. C. Microphotograph of the K-feldspar, containing coarse grain K-feldspar, quartz, amphibole and biotite. D. Microphotograph of the syenite, containing fine grain feldspar and quartz.

LA-ICPMS. The analytical method has been described in more detail by previous authors (Li et al., 2012a, 2012b; Liang et al., 2009; Tu et al., 2011). The whole rock trace element data were calculated by using ICPMSDataCal 7.0 (Liu et al., 2010).

3.2. Zircon U–Pb dating and zircon trace element analyses

Zircon grains were first separated through crushing samples to about 60 mesh, desliming in water, followed by density separation, magnetic separation and handpicking, then mounting in epoxy and polished down to near half sections to expose internal structures. Cathodoluminescent and optical microscopy images were taken in order to ensure that the least fractured, inclusion-free parts were analyzed. Zircon U–Pb dating and trace elements were analyzed using LA-ICPMS following the same technique as whole rock analyses (Li et al., 2012a, 2012b; Liang et al., 2009; Tu et al., 2011). The calculations of zircon isotope ratios and zircon trace elements were performed by ICPMSDataCal 7.0 (Liu et al., 2010). Zircon Ce anomalies were calculated by using software from the Research School of Earth Sciences, Australian National University (Ballard et al., 2002; Liang et al., 2006) and the zircon age was calculated using Isoplot (Version 3.23).

3.3. Zircon Lu–Hf isotopes

Zircon Lu–Hf isotope in-situ analysis was carried out at the State Key Laboratory of Continental Dynamics at Northwest University in Xi'an,

Table 1
Major and trace element results of Haiyang alkaline complex.

Sample	K-feldspar granite											Syenite											
	HY-01	HY-02	HY-03	HY-04	HY-05	HY-06	HY-07	HY-08	HY-09	HY-10	HY-11	HY-12	HY-13	HY-14	HY-15	HY-16	HY-17	HY-18	HY-19	HY-20	HY-21	HY-22	HY-23
SiO_2	68.5	69.8	69.3	69.4	67.2	68.3	68.4	68.7	64.4	68.6	70.7	72.0	71.2	72.3	72.5	72.4	73.4	73.0	72.1	73.3	73.3	72.1	72.1
TiO_2	0.38	0.31	0.36	0.34	0.39	0.35	0.38	0.36	0.37	0.41	0.31	0.18	0.21	0.19	0.18	0.21	0.18	0.19	0.18	0.19	0.18	0.19	0.19
Al_2O_3	15.2	14.8	14.8	14.9	15.4	15.0	15.1	14.7	16.1	14.8	14.2	13.7	14.1	13.8	13.6	13.9	13.7	13.6	13.7	13.9	13.8	13.8	13.5
Fe_2O_3	2.86	2.34	2.72	2.54	2.96	2.64	2.82	2.49	2.91	3.01	2.41	1.43	1.60	1.44	1.39	1.47	1.35	1.36	1.45	1.22	1.24	1.42	1.35
MnO	0.04	0.04	0.06	0.04	0.04	0.04	0.04	0.05	0.05	0.04	0.03	0.04	0.04	0.03	0.04	0.02	0.02	0.03	0.05	0.02	0.02	0.04	0.03
MgO	1.02	0.82	0.95	0.88	1.03	0.93	1.06	0.89	0.66	0.97	0.85	0.33	0.45	0.36	0.38	0.19	0.22	0.28	0.37	0.18	0.17	0.32	0.26
CaO	2.15	1.55	1.89	1.83	2.29	2.05	2.00	2.02	5.47	2.03	1.69	1.33	1.39	1.18	1.21	1.23	0.86	1.15	1.30	0.98	1.08	1.34	0.96
Na_2O	4.30	4.38	4.35	4.14	4.28	4.18	4.28	4.21	4.94	4.22	3.84	3.59	3.22	3.49	3.40	3.24	3.31	3.47	3.56	3.66	3.54	3.60	3.61
K_2O	4.36	4.60	4.16	4.74	4.50	4.62	4.57	4.51	3.00	4.26	4.65	4.97	5.00	4.77	4.91	5.12	5.04	4.88	4.82	4.69	4.79	4.83	4.64
P_2O_5	0.19	0.14	0.17	0.16	0.19	0.17	0.18	0.16	0.17	0.19	0.14	0.05	0.07	0.06	0.05	0.07	0.05	0.05	0.05	0.05	0.05	0.06	0.06
L.O.I.	0.69	0.84	0.92	0.69	1.34	1.34	0.78	1.54	1.63	1.14	0.79	1.99	2.39	1.96	2.05	1.68	1.48	1.64	2.04	1.43	1.47	1.96	2.99
Total	99.7	99.7	99.7	99.6	99.6	99.7	99.6	99.7	99.7	99.7	99.6	99.6	99.6	99.6	99.6	99.6	99.6	99.6	99.6	99.6	99.6	99.6	99.7
K_2O/Na_2O	1.01	1.05	0.96	1.15	1.05	1.11	1.07	1.07	0.61	1.01	1.21	1.38	1.55	1.37	1.45	1.58	1.52	1.41	1.35	1.28	1.35	1.34	1.29
Mg-number	41.5	41.1	41.2	41.0	40.9	41.4	42.9	41.7	31.2	39.2	41.2	31.6	36.2	33.4	35.1	20.3	24.2	29.0	34.0	23.2	21.8	31.1	27.5
Sc	4.01	3.20	3.58	3.05	3.84	4.10	4.16	3.31	3.92	4.14	2.44	2.17	2.03	2.05	2.11	2.09	1.99	2.52	1.97	2.05	2.26	2.17	2.02
Ti	2277	1847	2128	2035	2309	2078	2288	2175	2221	2428	1835	1081	1282	1167	1077	1263	1087	1125	1101	1109	1108	1139	1126
V	43.1	35.2	37.3	36.5	41.2	37.6	40.6	36.0	65.9	44.3	34.8	14.0	15.7	14.7	13.0	16.4	12.5	13.4	14.0	14.0	13.6	13.9	14.3
Cr	7.55	8.41	17.75	6.17	9.86	7.12	8.13	11.49	9.17	8.26	11.60	4.63	7.63	4.03	3.19	22.21	6.19	7.11	4.57	7.87	5.11	8.57	8.77
Mn	343	304	437	329	336	333	313	402	406	294	250	340	276	270	285	170	116	262	369	147	139	324	244
Co	5.25	4.24	4.74	4.29	4.71	4.10	4.34	3.58	3.12	3.86	2.97	2.03	2.10	2.00	2.20	2.31	2.02	2.21	2.38	1.74	1.96	1.96	2.16
Ni	6.49	4.74	11.73	9.15	6.22	8.65	6.19	5.14	5.40	4.35	10.41	3.28	4.07	3.87	2.64	4.92	2.68	4.43	3.46	4.65	2.46	4.38	4.02
Zn	51.2	33.2	47.4	31.2	51.4	46.8	48.4	52.0	39.2	40.3	36.0	39.8	44.2	34.7	40.3	43.3	38.3	40.5	45.7	38.2	42.1	43.0	49.0
Ga	27.2	27.4	26.7	28.6	29.2	27.5	28.1	25.4	29.6	25.7	22.8	21.2	22.3	21.2	20.0	22.8	19.5	19.4	19.9	20.0	19.8	20.0	21.3
Rb	83	90	86	88	85	87	106	100	59	103	100	113	111	89	101	112	105	110	102	101	101	105	94
Sr	461	399	412	477	460	421	453	385	836	401	354	170	204	187	173	191	168	164	170	156	158	166	156
Y	13.4	12.0	11.7	11.1	14.8	11.8	14.0	12.7	16.1	14.9	15.2	8.43	8.53	8.42	8.07	9.16	8.21	9.59	8.31	8.45	8.76	7.78	8.92
Zr	188	136	155	156	183	173	193	190	180	197	156	120	133	122	114	141	116	128	118	120	120	119	119
Nb	12.5	10.3	11.4	10.4	12.2	11.6	13.5	13.1	14.1	13.6	11.2	10.4	10.2	10.6	9.9	10.7	10.8	11.6	10.4	10.6	10.5	9.8	10.9
Ba	1300	1205	1085	1293	1322	1224	1355	1182	1355	1113	852	811	931	842	825	1032	728	713	825	810	804	808	791
La	62.7	45.8	41.3	48.7	45.8	41.6	50.1	48.8	51.2	54.9	37.0	35.0	37.9	37.4	35.7	37.8	31.8	37.2	34.9	36.6	34.9	34.7	36.2
Ce	95.1	74.7	70.9	77.4	79.9	71.9	84.7	82.6	89.0	91.2	66.0	52.4	57.5	56.7	53.9	58.2	50.3	57.0	53.2	55.8	53.7	54.2	54.6
Pr	8.91	7.34	7.49	7.65	8.09	7.30	8.34	8.31	9.12	9.16	6.94	5.00	5.17	5.11	4.97	5.32	4.79	5.08	4.90	5.21	4.77	4.83	4.94
Nd	31.9	26.7	25.4	26.1	30.3	26.4	29.9	28.8	33.5	32.6	25.8	16.7	18.3	18.1	17.6	19.0	17.1	17.6	17.2	17.7	17.4	16.9	17.6
Sm	4.63	3.67	3.88	3.85	4.26	3.71	4.47	4.12	5.14	4.67	4.35	2.45	2.47	2.83	2.24	2.85	2.29	2.74	2.60	2.57	2.41	2.26	2.41
Eu	0.87	0.80	0.71	0.83	0.90	0.86	0.85	0.81	0.97	0.88	0.79	0.45	0.51	0.51	0.44	0.43	0.42	0.43	0.49	0.48	0.45	0.42	0.50
Gd	3.46	3.40	3.17	3.43	3.53	3.27	3.40	2.96	3.46	3.64	3.35	2.10	2.08	1.87	1.73	2.06	2.08	1.99	2.09	1.87	2.20	1.83	2.07
Tb	0.39	0.30	0.31	0.36	0.42	0.32	0.42	0.40	0.45	0.41	0.47	0.21	0.26	0.24	0.24	0.27	0.23	0.24	0.24	0.23	0.27	0.22	0.25
Dy	2.28	2.21	1.93	1.93	2.47	2.07	2.46	2.31	2.81	2.73	2.56	1.58	1.47	1.71	1.54	1.56	1.50	1.59	1.45	1.39	1.24	1.29	1.63
Ho	0.45	0.35	0.37	0.32	0.49	0.35	0.48	0.40	0.53	0.49	0.46	0.30	0.33	0.27	0.23	0.32	0.26	0.27	0.27	0.27	0.28	0.26	0.25
Er	1.37	1.12	1.03	0.95	1.33	1.18	1.38	1.24	1.57	1.45	1.53	0.85	0.80	0.84	0.85	1.09	0.82	0.99	0.83	0.84	0.92	0.72	0.91
Tm	0.21	0.16	0.13	0.25	0.21	0.17	0.20	0.18	0.22	0.21	0.22	0.13	0.13	0.14	0.11	0.15	0.12	0.13	0.14	0.15	0.14	0.13	0.14
Yb	1.45	1.32	1.21	1.17	1.32	1.37	1.50	1.31	1.66	1.68	1.44	1.05	1.27	0.87	1.05	1.06	0.91	1.39	1.26	1.11	1.23	0.96	1.00
Lu	0.23	0.19	0.27	0.14	0.27	0.16	0.25	0.20	0.23	0.26	0.24	0.19	0.15	0.17	0.16	0.22	0.15	0.20	0.14	0.14	0.15	0.12	0.19
Hf	5.26	3.81	4.42	4.18	4.96	4.72	5.27	4.81	4.86	5.16	3.98	4.53	4.15	3.86	3.73	4.47	3.79	4.09	3.83	3.69	3.64	3.88	3.90
Ta	0.84	0.77	0.82	0.75	0.94	0.86	1.06	0.96	1.04	0.99	0.99	0.95	0.88	0.91	0.92	0.88	1.00	1.06	0.94	0.93	0.93	0.83	0.98
Pb	14.7	15.5	17.5	14.2	13.4	13.7	14.6	18.0	12.8	13.2	14.4	17.4	13.0	11.8	15.5	18.3	22.5	18.3	27.9	22.9	12.6	22.7	21.5
Th	17.8	15.7	19.9	15.1	19.4	15.4	21.7	19.8	16.4	24.0	16.1	12.1	10.8	11.9	11.5	11.8	12.9	13.7	11.6	12.4	12.1	11.3	12.6
U	2.40	2.04	2.84	1.84	4.07	3.01	3.64	3.82	2.14	4.16	2.51	2.25	2.94	2.81	2.17	2.38	1.95	2.75	3.17	1.99	1.87	1.97	3.18

Wt.% for major element and ppm for trace element.

using a Geolas-193 laser ablation microprobe coupled with a Nu plasma high-resolution (HR) Multi-Collector (MC)-ICPMS. The analytical procedures followed the description from Yuan et al. (2008). The conditions were laser energy density of 15–20 J/cm^2 and a repetition rate of 10 Hz with a spot size of 44 μm in diameter and ablation time of 40 s. As Woodhead et al. (2004) advocated, the isobaric interference-free ^{176}Yb on ^{176}Hf was corrected by measuring the interference-free ^{172}Yb and ^{173}Yb, calculating mean βYb value from ^{172}Yb and ^{173}Yb, and using the recommended ^{176}Yb/^{172}Yb ratio of 0.5886 (Chu et al., 2002). The isobaric interference of ^{176}Lu on ^{176}Hf was corrected by measuring the intensity of the interference-free ^{175}Lu isotope, and using a recommended ^{176}Lu/^{177}Hf ratio of 0.02669 (De Biévre and Taylor, 1993) to calculate ^{176}Lu/^{177}Hf ratios. Zircon 91,500 was used as the reference standard, with a recommended ^{176}Hf/^{177}Hf ratio of 0.282306 ± 10 (Woodhead et al., 2004). All the Lu–Hf isotope analysis results are reported with 2σ errors.

We adopted a decay constant for ^{176}Lu of 1.867×10^{-11} year^{-1} (Soderlund et al., 2004). Initial ^{176}Hf/^{177}Hf ratios $\varepsilon_{Hf}(t)$ were calculated with reference to the chondritic reservoir (CHUR) (BlichertToft et al., 1997) at the time of zircon growth in the magma. The single stage Hf model age (T_{DM1}) is calculated relative to the depleted mantle with present-day ^{176}Hf/^{177}Hf = 0.28325 and ^{176}Lu/^{177}Hf = 0.0384 (Griffin et al., 2000). Two-stage Hf model age (T_{DM2}) is calculated with the average continental crust ^{176}Lu/^{177}Hf ratio of 0.015 (Griffin et al., 2002).

3.4. Zircon O isotope

Zircon O isotope analyses were performed on a Sensitive High Resolution Ion MicroProbe multiple collector instrument (SHRIMP IIe MC) at the Beijing SHRIMP center. During the analysis, Cs^+ primary ion beam was focused to a diameter of 25 μm on the target surface with primary current of ~2 nA, generating approximately 250 pA of O^- secondary ions which were then accelerated by −10 kV with a normal-incidence electron gun for charge compensation (Trotter et al., 2008). The electron beam is adjusted to provide the highest intensity secondary ion current. Simultaneous ^{16}O and ^{18}O measurement was achieved by use of two Faraday cups equipped with 10^{10} and 10^{11} Ω resistor amplifiers, respectively. Data were corrected for instrumental mass fractionation using the zircon standard Temora (Ickert et al., 2008) mounted in the sample mount. Standards were measured every 3 sample analyses. Oxygen isotope ratios are reported in standard permil notation relative to Vienna Standard Mean Ocean Water (VSMOW) with 2σ errors.

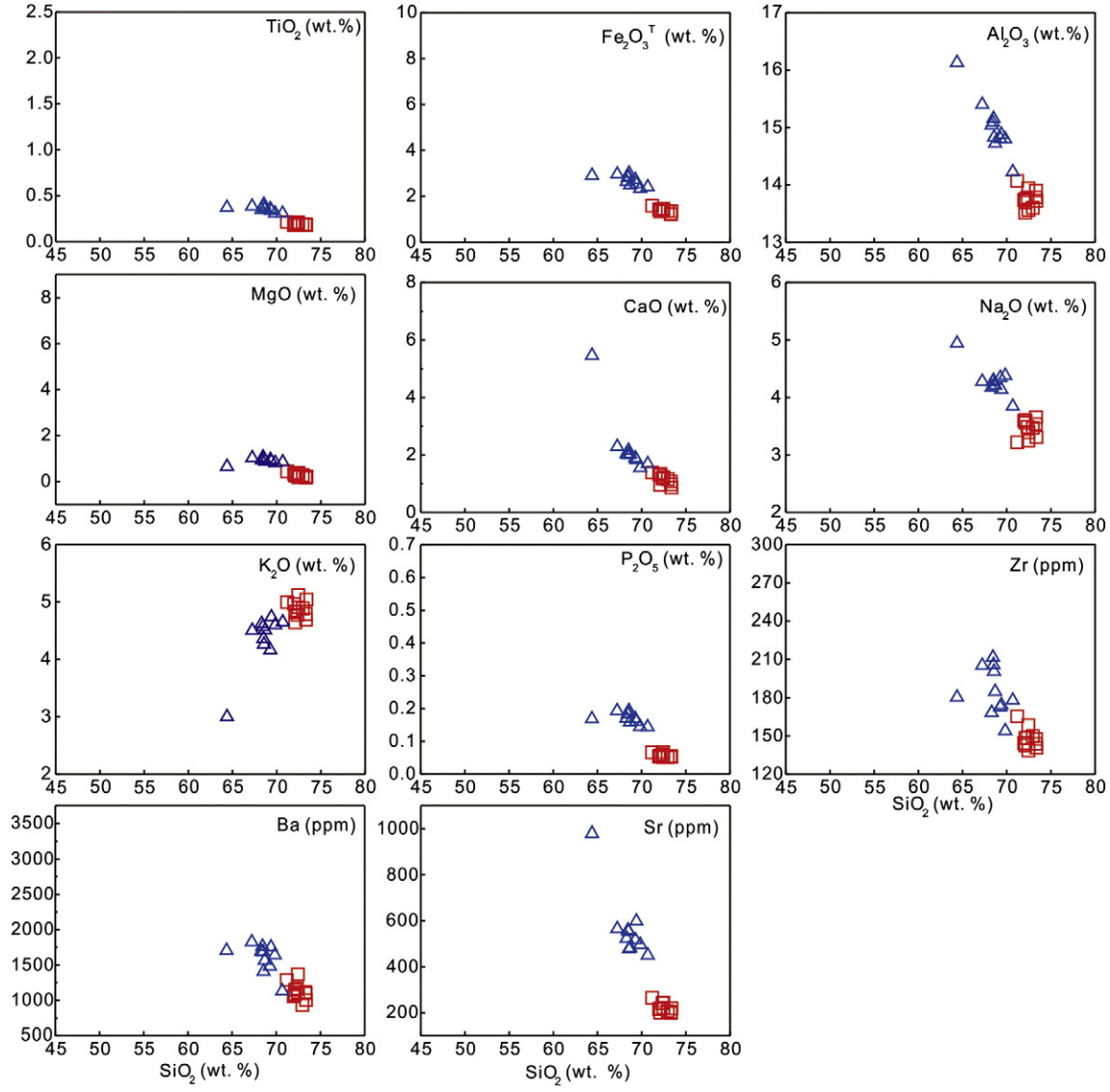

Fig. 3. Harker diagrams for K-feldspar granite and Haiyang syenite samples. The hollow triangle stands for K-feldspar granite and the quadrate stands for syenite. Symbols are the same as Fig. 4.

3.5. Apatite major and trace element analyses

Fluorine and Cl compositions of apatite from the Haiyang massif rocks were determined by a JXA-8100 electron microprobe at the State Key Laboratory of Mineral Deposits Research, Nanjing University. The analyzing conditions were 15 keV and 10 nA current, with a 10 μm diameter electron beam. Norbergite was used as standard for F, and $Ba_5(PO_4)_3Cl$ for Cl, apatite for Ca and P standards. Counting times were 20 s for Si, Al, Mg, Fe, Mn, Ca, Sr, and P and reduce to 10 s for F and Cl to avoid volatile loss. Fluorine was determined using Kα line obtained with a LDE1 crystal and chlorine was determined using Kα line obtained with a PET crystal. Detail method was described previously (Li et al., 2012a).

The apatite trace element analyses were also carried out using LA-ICPMS at the State Key Laboratory of Isotope Geochemistry, Guangzhou Institute of Geochemistry, Chinese Academy of Sciences. The conditions were 80 mJ laser energy and a repetition rate of 6 Hz with a spot size of 41 μm in diameter and 40 s ablation time. NIST 612 was used as standard, NIST 610 was used as monitoring standard, and ^{43}Ca was used as internal standard (Li et al., 2012a, 2012b; Liang et al., 2009; Tu et al., 2011). The calculations of the apatite trace elements were performed by ICPMSDataCal 7.0 (Liu et al., 2008).

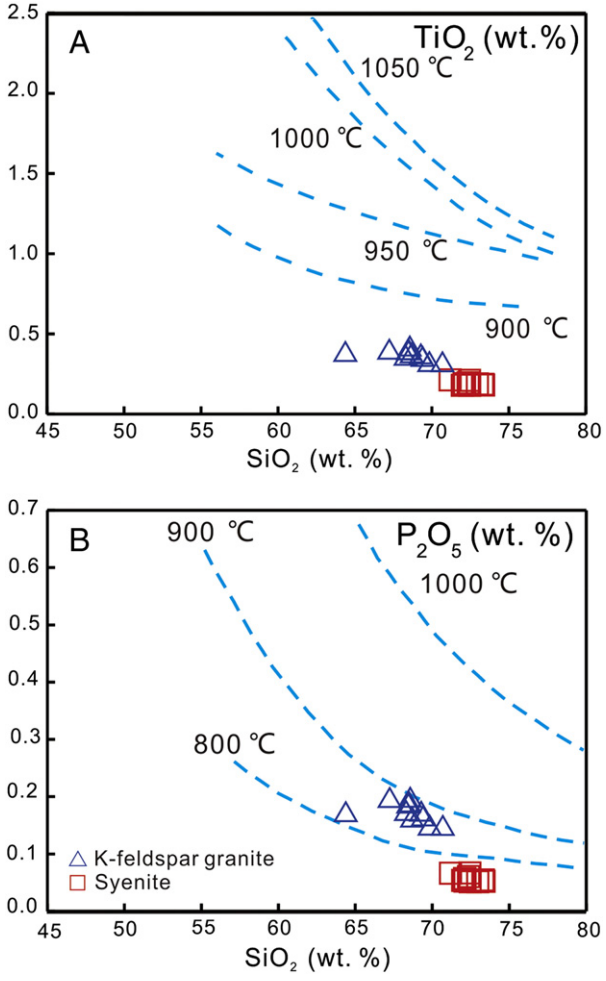

Fig. 4. A. TiO_2 vs SiO_2 diagram for Haiyang alkaline complex (Green and Pearson, 1986) showing all samples formed less than 900 °C; B. P_2O_5 vs SiO_2 diagram for Haiyang plutons (Harrison and Watson, 1984) showing K-feldspar granites formed higher than 800 °C, while syenite less than 800 °C.

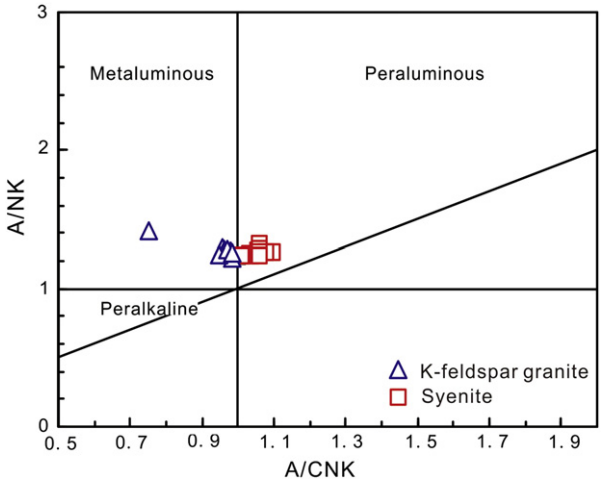

Fig. 5. A/NK versus A/CNK diagram for Haiyang alkaline complex samples. K-feldspar granite shows metaluminous nature and syenite shows a slightly peraluminous nature. A/NK = Al/(Na + K) (molar ratio). A/CNK = Al/(Ca + Na + K) (molar ratio). Symbols are the same as Fig. 4.

4. Results

4.1. Whole-rock major and trace elements

Twenty three samples from the Haiyang granite complex were analyzed for major and trace element compositions, including eleven K-feldspar granite samples and twelve syenite samples. The major and trace element data are summarized in Table 1. In Harker diagrams, TiO_2, Al_2O_3, Fe_2O_3, MgO, CaO, and P_2O_5 contents and Sr, Ba and Zr concentrations of Haiyang K-feldspar granite and syenite are negatively

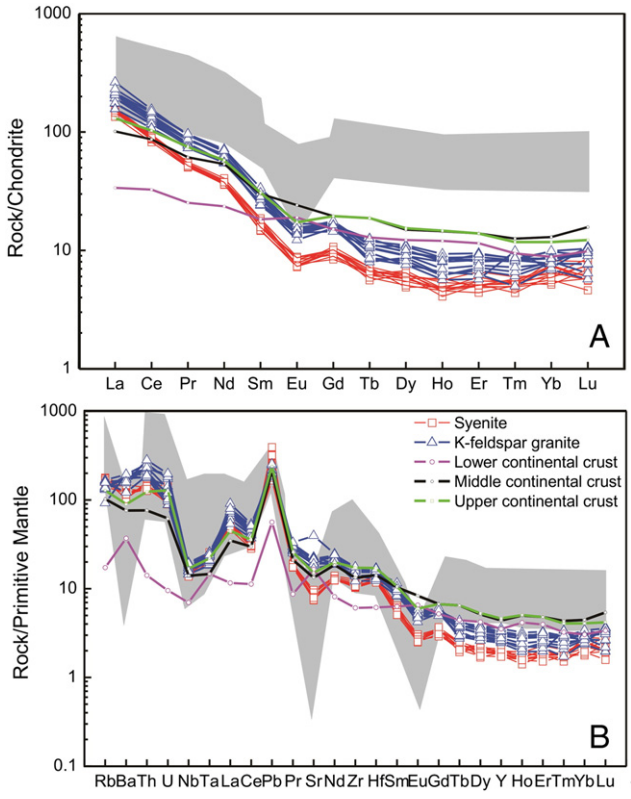

Fig. 6. A. Chondrite-normalized REE diagram. Chondritic values were from Sun and McDonough (1989); B. Primitive mantle-normalized trace element diagram. Primitive mantle values were from Sun and McDonough (1989). The shadow area stands for data of the LYR belt.

correlated with SiO_2, whereas K_2O increases with SiO_2 (Fig. 3). The formation temperature of these samples are slightly less than 900 °C as indicated by whole rock Ti thermometer (Fig. 4A). Whole rock P thermometer, however, shows that the formation temperature of K-feldspar granite is systematically higher than that of the syenite, which is less than 800 °C (Fig. 4B).

4.1.1. K-feldspar granite

K-feldspar granite samples have high SiO_2 (64.4–70.7 wt.%), Na_2O (3.84–4.94 wt.%), and K_2O (3.0–4.74 wt.%) contents and low TiO_2 (0.31–0.41 wt.%), Al_2O_3 (14.2–16.1 wt.%), Fe_2O_3 (2.34–3.01 wt.%), MgO (0.66–1.06 wt.%), CaO (1.55–5.47 wt.%) and P_2O_5 (0.14–0.19 wt.%) contents. The SiO_2 contents, $FeO_T/(FeO_T + MgO)$ ratios (0.71–0.80) and K_2O/Na_2O ratios (0.61–1.21) are lower than those of the Haiyang syenite (0.76–0.87, 1.28–1.58). They are metaluminous with A/CNK ratios from 0.7 to 0.99 (Fig. 5) and alkaline-calcic rocks. The total alkali ($K_2O + Na_2O$) ranges from 7.94 to 8.98 wt.% and the Na_2O/K_2O ratios are a little higher than that of the syenite (0.87–0.99).

The Haiyang K-feldspar granite is characterized by high concentrations of large iron lithophile elements (LILE) such as Na, K, Rb, and Ba, and high field strength elements (HFSE) such as Zr, Hf, Th and U (Table 1). According to the chondrite-normalized REE diagram, they are enriched in light rare earth elements (LREEs) and depleted in heavy rare earth elements (HREEs) ($(La/Yb)_{CN} = 18.4$ to 31.1) with slightly negative Eu-anomalies (Fig. 6A). The REE concentrations are lower than those of the LYR belt, especially the HREEs lower than the upper continental crust. In spider diagram, they are similar to the upper continental crust (UCC). But they have higher Rb, Ba, Th, U, and La concentrations than the UCC with strongly positive Pb anomaly, indicating an enriched source. Slight Ba and Eu anomalies indicating limited plagioclase crystallization.

4.1.2. Syenite

The Haiyang syenite has high SiO_2 (71.2–73.4 wt.%), Na_2O (3.22–3.66 wt.%), and K_2O (4.64–5.12 wt.%) contents and low TiO_2 (0.18–0.21 wt.%), Al_2O_3 (13.5–14.1 wt.%), Fe_2O_3 (1.22–1.60 wt.%), MgO (0.96–1.39 wt.%), CaO (0.86–1.39 wt.%) and P_2O_5 (0.05–0.07 wt.%) contents. They are slightly peraluminous (Fig. 5) with A/CNK ratios ranging from 1.01 to 1.10, and are alkaline-calcic rocks with high $K_2O + Na_2O$ (8.22–8.56 wt.%) and low Na_2O/K_2O ratios (0.63–0.78).

The syenite samples are also enriched in Na, K, Rb, Ba, Sr, La, Th, and U and depleted in Nb and Ta. The total REE concentrations are lower than the K-feldspar granite (Fig. 6A), with $(La/Yb)_{CN}$ ratios ranging from 19.2 to 30.7. In a primitive mantle-normalized trace element diagram, the Haiyang syenite shows a similar pattern to the K-feldspar granite, but with more depleted HREE with stronger negative Sr and Eu anomalies (Fig. 6B).

4.2. Geochronology

Zircons from samples HY-01 (K-feldspar granite) and HY-18 (syenite) have been dated using LA-ICPMS. They are mostly prismatic, transparent, pale yellow in color, and ranging from 100 to 200 μm in size with a clear zonal growth structure revealed in their CL images, typical for igneous zircons. Inherited cores are rare, which are surrounded by prismatic and transparent rims (Fig. 7). The zircon U–Pb isotopic data and trace elements data are summarized in Tables 2 and 3, and illustrated in the concordia diagram and zircon chondrited-normalized REE diagram (Fig. 8).

4.2.1. K-feldspar granite zircon

Twenty analyses for zircon from the sample HY-01 were undertaken. The U and Th concentrations of zircon grains range from 256 to 872 ppm and from 186 to 2261 ppm, respectively (Table 3). The Th/U ratios range from 0.66 to 2.64, compatible with a magmatic origin (Belousova et al., 2002; Hoskin and Black, 2000; Sun et al., 2002). The twenty zircon grains have ages ranging from 110 Ma to 122 Ma and yield a weighted mean $^{206}Pb/^{238}U$ age of 116.8 ± 1.7 Ma (Fig. 7; Table 2), which represents the crystallization age of the K-feldspar granite. Zircon Ce(IV)/Ce(III) ratios range from 33 to 825, indicating highly varied but relatively high oxygen fugacities. According to Ti concentrations in zircons, the temperature of zircon ranges from 620 to 760 °C (Table 2). This temperature is lower than whole rock P thermometer (800–900 °C) (Fig. 4) and slightly lower than zircon Ti temperature of A_2-type granites in LYR Belt, ranging from 650 to 800 °C (Li et al., 2012b). This may imply that these Haiyang K-feldspar granite zircons crystallized late during magma evolution, likely due to high alkaline contents.

4.2.2. Syenite zircon

Sixteen analyses from sample HY-18 were undertaken. The U concentration ranges from 69 to 1143 ppm and the Th concentration from 85 to 3524 ppm (Table 3), with Th/U ratios ranging from 0.62 to 3.24, compatible magmatic origin (Belousova et al., 2002; Hoskin and Black, 2000; Sun et al., 2002). Thirteen zircon grains have ages ranging from 112.0 Ma to 119.2 Ma and yielding a weighted mean $^{206}Pb/^{238}U$ age of 115.8 ± 2 Ma, which is taken as the crystallization age of the syenite (Fig. 7). This age is marginally younger than that of the K-feldspar

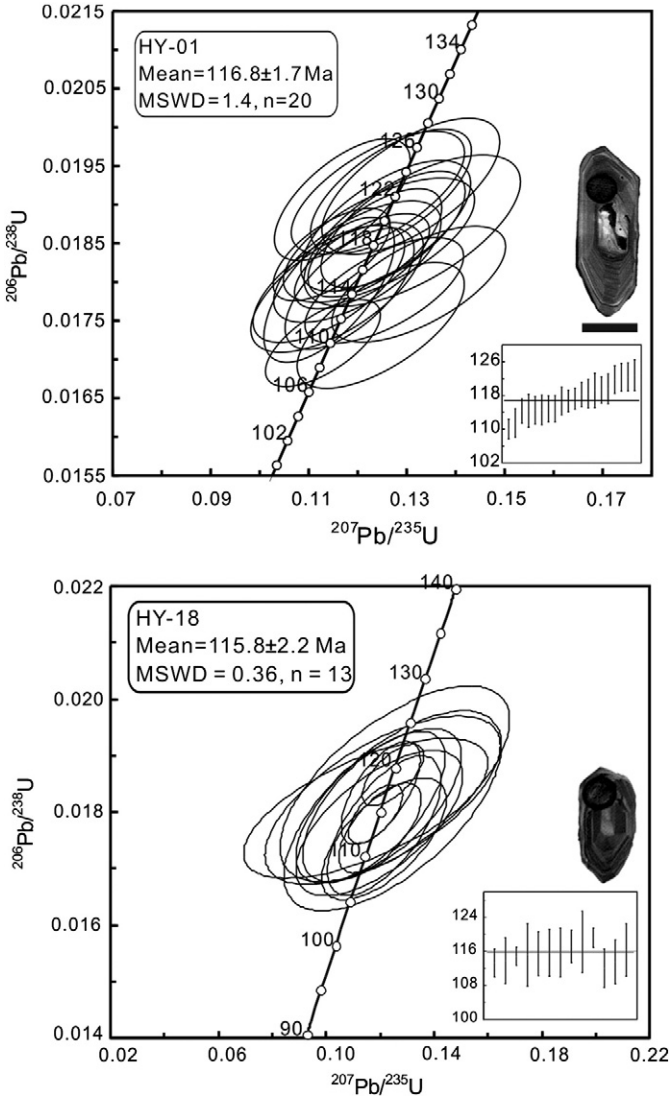

Fig. 7. Zircon U–Pb concordia diagrams of Haiyang K-feldspar granite (HY-01) and syenite (HY-18). The average mean age of K-feldspar granite is marginally the same as but slightly older than the syenite.

Table 2
LA-ICPMS zircon U–Pb isotope composition and age of the Early Cretaceous Haiyang A-type granite complex.

Sample	$^{207}Pb/^{235}U$	$^{207}Pb/^{235}U$	$^{206}Pb/^{238}U$	$^{206}Pb/^{238}U$	$^{206}Pb/^{238}U$	$^{206}Pb/^{238}U$	Pb	Th	U	Th/U	Ce^{4+}/Ce^{3+}	T
	Ratio	2sigma	Ratio	2sigma	Age (Ma)	2sigma	ppm	ppm	ppm			°C
HY-01-01	0.1254	0.0107	0.0179	0.0005	114.3	2.9	9.05	385	388	0.99	445	680
HY-01-02	0.1183	0.0087	0.0179	0.0005	114.5	3.3	11.38	474	513	0.92	479	680
HY-01-03	0.1142	0.0088	0.0179	0.0006	114.4	3.9	8.04	430	325	1.32	275	723
HY-01-04	0.1235	0.0090	0.0185	0.0005	118.2	2.9	19.00	829	806	1.03	440	691
HY-01-05	0.1325	0.0117	0.0180	0.0005	114.8	3.1	9.45	374	407	0.92	272	648
HY-01-06	0.1241	0.0117	0.0192	0.0005	122.3	3.3	5.92	186	261	0.71	825	681
HY-01-07	0.1129	0.0077	0.0172	0.0004	110.0	2.4	16.63	1409	534	2.64	33	722
HY-01-08	0.1209	0.0091	0.0183	0.0004	116.7	2.6	9.81	388	416	0.93	460	624
HY-01-09	0.1272	0.0097	0.0187	0.0005	119.3	3.1	10.33	561	395	1.42	384	673
HY-01-10	0.1147	0.0079	0.0184	0.0004	117.3	2.5	27.99	2261	872	2.59	110	734
HY-01-11	0.1169	0.0091	0.0191	0.0005	121.7	3.3	18.54	1413	572	2.47	58	694
HY-01-12	0.1309	0.0120	0.0192	0.0006	122.8	3.7	10.79	424	438	0.97	708	657
HY-01-13	0.1247	0.0113	0.0174	0.0005	111.5	3.4	6.96	278	328	0.85	489	640
HY-01-14	0.1311	0.0146	0.0187	0.0006	119.2	4.1	7.43	345	291	1.18	246	713
HY-01-15	0.1141	0.0102	0.0180	0.0005	114.9	3.2	10.19	496	426	1.16	383	656
HY-01-16	0.1158	0.0116	0.0179	0.0006	114.6	3.5	7.48	504	271	1.86	202	729
HY-01-17	0.1243	0.0129	0.0185	0.0005	118.4	3.3	7.66	578	256	2.25	87	754
HY-01-18	0.1257	0.0114	0.0187	0.0006	119.6	3.5	6.46	195	296	0.66	599	629
HY-01-19	0.1268	0.0108	0.0192	0.0005	122.4	3.4	12.22	804	425	1.89	209	693
HY-01-20	0.1199	0.0113	0.0183	0.0005	116.7	3.3	9.21	375	403	0.93	381	685
HY-18-01	0.1199	0.0100	0.0177	0.0005	113.2	3.3	19.34	1224	715	1.71	57	701
HY-18-02	0.1246	0.0266	0.0180	0.0012	115.2	7.4	1.69	85	69	1.24	24	635
HY-18-03	0.1196	0.0204	0.0178	0.0008	113.8	5.4	4.88	396	154	2.57	1	794
HY-18-04	0.1202	0.0097	0.0183	0.0006	117.2	3.8	12.46	1166	360	3.24	43	769
HY-18-05	0.1213	0.0153	0.0175	0.0007	112.0	4.5	4.15	129	209	0.62	97	621
HY-18-06	0.1215	0.0139	0.0178	0.0008	113.5	5.2	3.65	184	146	1.26	98	694
HY-18-07	0.1254	0.0281	0.0185	0.0011	118.2	7.2	2.83	177	95	1.86	68	745
HY-18-08	0.1193	0.0202	0.0181	0.0009	115.7	5.7	3.88	146	153	0.95	52	769
HY-18-09	0.1146	0.0299	0.0181	0.0008	115.4	5.2	3.76	181	135	1.35	49	738
HY-18-10	0.1182	0.0067	0.0180	0.0003	114.8	2.2	43.34	3524	1443	2.44	120	783
HY-18-11	0.1247	0.0075	0.0187	0.0004	119.2	2.3	28.20	1876	970	1.93	56	748
HY-18-12	0.1177	0.0175	0.0181	0.0009	115.7	5.5	4.79	229	177	1.30	30	737
HY-18-13	0.1209	0.0288	0.0182	0.0010	116.3	6.2	1.73	87	75	1.17	43	728

Table 3
Zircon trace element data for Haiyang A-type granite complex.

Sample	La (ppm)	Ce	Pr	Nd	Sm	Eu	Gd	Tb	Dy	Ho	Er	Tm	Yb	Lu	Hf
HY-01-01	0.21	87.8	0.16	2.11	3.98	1.01	21.8	8.30	106	43.9	218	50.0	494	101	11231
HY-01-02	1.00	73.0	0.25	2.32	3.58	0.78	20.3	7.69	102	43.7	223	52.5	526	106	11,561
HY-01-03	0.16	128	0.20	3.62	6.36	1.73	33.1	11.4	144	56.4	261	58.1	548	109	8720
HY-01-04	0.04	100	0.16	2.29	4.47	1.24	24.6	8.59	106	41.8	212	51.3	528	108	10,837
HY-01-05	10.2	81.2	2.66	10.8	4.75	0.82	20.4	7.30	95.7	38.6	194	45.9	462	92.8	11,577
HY-01-06	0.01	37.4	0.04	0.49	1.53	0.36	10.1	3.70	51.2	22.2	119	29.7	308	65.3	11,991
HY-01-07	0.14	229	1.12	17.4	28.5	10.7	112	31.0	323	108	445	89.7	791	149	8748
HY-01-08	0.00	57.0	0.06	1.31	3.22	0.48	18.6	7.03	96.4	41.0	213	51.1	510	105	12,402
HY-01-09	0.00	79.4	0.12	1.74	3.33	1.10	20.3	6.61	82.6	32.9	151	34.4	336	67.7	11,084
HY-01-10	0.07	314	0.61	9.74	18.8	4.70	87.5	25.5	284	101	432	89.2	811	154	7940
HY-01-11	0.18	334	1.09	16.6	28.5	7.74	117	34.0	363	124	513	103	917	174	7990
HY-01-12	0.00	59.9	0.05	1.14	2.23	0.42	15.0	5.57	76.2	31.4	160	37.6	374	75.5	11,845
HY-01-13	0.03	49.1	0.03	1.27	2.25	0.39	12.6	4.75	60.6	25.8	129	31.5	314	62.7	11,905
HY-01-14	0.00	59.5	0.13	1.22	3.53	1.01	18.4	5.95	73.2	29.0	138	32.3	316	63.7	10,503
HY-01-15	0.05	65.6	0.10	1.65	3.04	0.65	16.1	5.72	71.9	30.6	147	34.8	337	67.0	11,713
HY-01-16	0.35	186	0.45	6.48	10.2	4.01	52.3	17.6	210	82.1	371	78.5	729	142	7689
HY-01-17	0.07	190	0.67	9.72	16.0	5.89	74.2	21.4	243	90.2	395	81.5	741	144	7255
HY-01-18	0.02	33.5	0.02	0.49	1.73	0.32	10.4	3.69	52.7	22.8	121	29.8	320	66.6	11,538
HY-01-19	0.25	135	0.27	3.71	6.97	2.25	35.8	11.7	136	51.7	235	51.5	478	93.9	10230
HY-01-20	1.28	60.3	0.38	2.90	3.44	0.73	19.2	6.92	89.9	38.1	191	45.0	459	93.3	11,608
HY-18-01	0.53	203	1.16	14.6	21.4	5.35	92.3	28.8	333	128	587	129	1233	240	9940
HY-18-02	0.07	29.3	0.14	4.03	6.24	1.93	25.4	7.97	93.6	34.7	158	33.7	312	61.8	9363
HY-18-03	0.71	155	5.56	79.1	85.5	40.2	236	59.4	536	166	645	125	1103	204	7827
HY-18-04	3.83	201	1.35	13.0	17.9	7.76	79.0	22.8	244	85.0	362	74.3	687	130	7693
HY-18-05	0.00	20.6	0.04	0.73	2.57	0.76	15.1	5.43	68.0	27.8	131	29.3	293	60.5	12,111
HY-18-06	5.10	72.1	1.43	7.57	5.72	1.51	24.7	8.30	102	41.1	191	43.0	410	83.2	9054
HY-18-07	0.08	80.2	0.21	4.15	6.66	3.11	33.6	10.5	117	43.7	193	39.9	363	71.9	7718
HY-18-08	0.02	46.0	0.31	4.47	7.32	3.16	36.3	12.7	152	60.1	279	61.3	585	117	7855
HY-18-09	3.93	63.4	0.84	6.65	8.10	2.34	35.1	11.3	132	51.9	235	50.7	480	96.6	8949
HY-18-10	0.01	510	0.72	11.6	24.7	8.02	121	37.6	422	156	692	147	1381	267	9082
HY-18-11	0.11	304	1.04	15.0	27.7	7.78	120	36.8	419	156	695	148	1387	263	9358
HY-18-12	0.13	69.1	0.47	6.58	10.6	3.54	39.9	11.9	135	50.7	221	48.6	453	92.1	8663
HY-18-13	0.02	29.8	0.18	3.14	5.08	1.92	22.3	7.03	84.6	33.7	157	35.0	339	71.0	7999

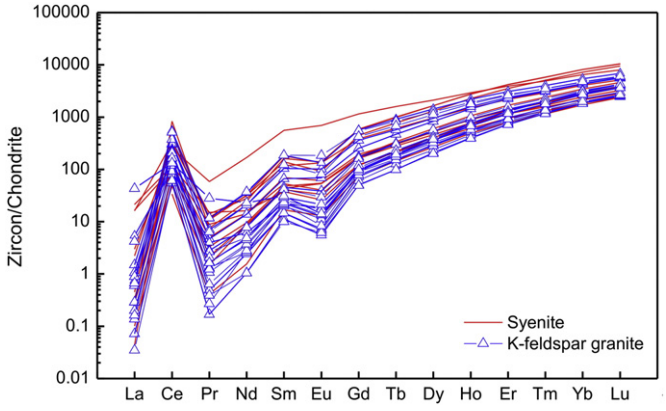

Fig. 8. Zircon chondrite-normalized REE diagram. Chondritic values were from Sun and McDonough (1989). There is strongly Eu positive anomaly indicating formed at relatively high oxygen fugacity environment.

granite, which is consistent with field observations, i.e. the syenite intruded into the K-feldspar granite. Two zircon grains have $^{206}Pb/^{238}U$ ages of 125.8 Ma and 127.9 Ma (Ce^{4+}/Ce^{3+} = 111.3, 28.3), and one old zircon grain with $^{206}Pb/^{238}U$ age of 552.7 Ma. These are inherited zircons, representing previous magmatic events. Zircon Ce^{4+}/Ce^{3+} ratios range from 24.1 to 120.5, indicating the granites formed at low oxygen fugacity (Ballard et al., 2002; Liang et al., 2006) than the K-feldspar granite. The Ti concentrations in zircon thermometer yield temperatures ranging from 620 to 780 °C (Table 2). This temperature is lower than that of whole rock P thermometer (800 °C) (Fig. 4).

4.3. Zircon Hf isotope and O isotope

Zircons dated for U–Pb ages were also analyzed for Lu–Hf isotopes, and the results are given in Table 4. Initial $^{176}Hf/^{177}Hf$ ratios, denoted as $\varepsilon_{Hf}(t)$ values, and Hf model ages were also calculated based on crystallization ages from the U–Pb dating (Table 4). Zircon grains from the Haiyang K-feldspar granite (HY-01) have large variation of $^{176}Hf/^{177}Hf$ ratios from 0.282068 to 0.282262 and $\varepsilon_{Hf}(t)$ values mainly from −22.6 to −15.6 (Fig. 9). Correspondingly, their two-stage Hf model

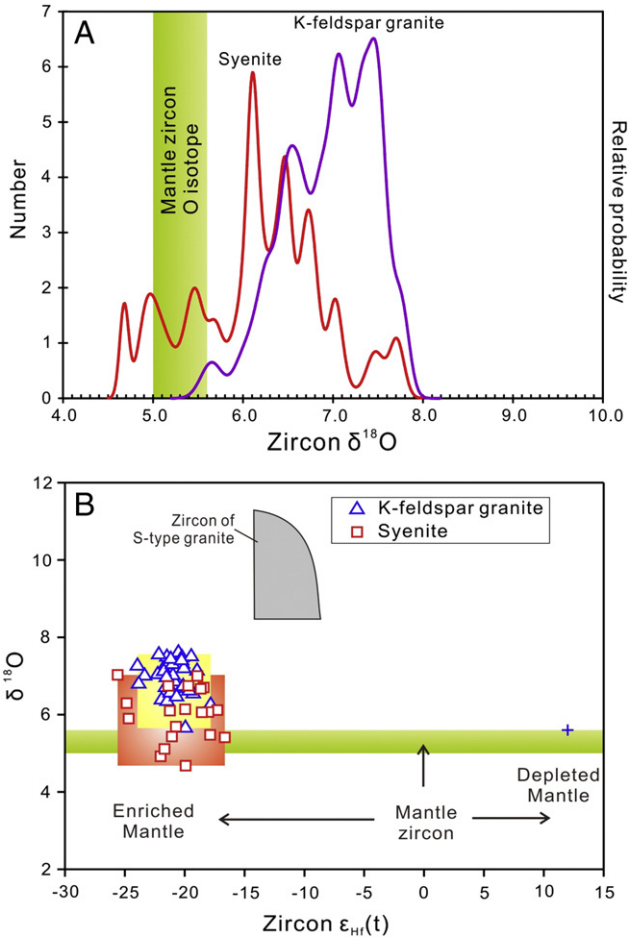

Fig. 9. A. Zircon $\delta^{18}O$ frequency diagram for Haiyang alkaline complex; B. zircon $\varepsilon_{Hf}(t)$ vs zircon $\delta^{18}O$ diagram for Haiyang alkaline complex. The shaded field depicts the zircon Hf–O isotope compositions of zircons from the S-type granites from Li et al. (2009). Zircon $\delta^{18}O$ data of mantle is from Valley et al. (1998). The red and the yellow field represent the zircon Hf–O isotope compositions the Haiyang syenite and the K-feldspar granite.

Table 4
Lu–Hf isotope data for zircon from the Haiyang A-ty the pe granite complex.

Sample	T(Ma)	Lu	Hf	Lu/Hf	$^{176}Hf/^{177}Hf$	2S	$^{176}Yb/^{177}Hf$	$^{176}Lu/^{177}Hf$	$^{176}Hf/^{177}Hf(i)$	$\varepsilon_{Hf}(T)$	T_{DM1}	T_{DM2}
HY-01-01	114.3	109	8720	0.012518	0.282108	0.000020	0.042064	0.001700	0.282105	−21.1	1641	2204
HY-01-02	114.5	92.8	11577	0.008012	0.282103	0.000018	0.030317	0.001236	0.282100	−21.2	1628	2212
HY-01-03	114.4	108	10837	0.009995	0.282136	0.000018	0.020843	0.000870	0.282134	−20.1	1567	2148
HY-01-04	118.2	75.5	11845	0.006371	0.282262	0.000024	0.032864	0.001349	0.282259	−15.6	1410	1903
HY-01-05	114.8	149	8748	0.016994	0.282153	0.000019	0.022877	0.000958	0.282151	−19.4	1546	2114
HY-01-07	110.0	101	11231	0.008971	0.282160	0.000019	0.019993	0.000841	0.282158	−19.3	1532	2102
HY-01-08	116.7	154	7940	0.019399	0.282225	0.000019	0.022617	0.000931	0.282223	−16.8	1445	1973
HY-01-09	119.3	67.0	11713	0.005723	0.282068	0.000018	0.025475	0.001026	0.282066	−22.4	1667	2277
HY-01-10	117.3	174	7990	0.021786	0.282120	0.000019	0.025510	0.001026	0.282118	−20.6	1595	2178
HY-01-11	121.7	144	7255	0.019849	0.282139	0.000021	0.023074	0.000964	0.282137	−19.8	1566	2138
HY-01-12	122.8	93.3	11608	0.008035	0.282205	0.000021	0.017295	0.000738	0.282203	−17.4	1466	2010
HY-01-14	119.2	63.7	10503	0.006063	0.282214	0.000024	0.047670	0.001928	0.282209	−17.3	1501	1998
HY-01-15	114.9	105	12402	0.008504	0.282095	0.000025	0.032905	0.001339	0.282092	−21.5	1643	2228
HY-01-16	114.6	65.3	11991	0.005443	0.282200	0.000023	0.034662	0.001390	0.282197	−17.8	1498	2025
HY-18-02	115.2	61.8	9363	0.006599	0.282200	0.000018	0.025382	0.001037	0.282198	−17.8	1484	2023
HY-18-03	113.8	204	7827	0.026034	0.282150	0.000021	0.049389	0.001952	0.282146	−19.6	1592	2123
HY-18-04	117.2	130.5	7693	0.016961	0.282315	0.000020	0.070768	0.002820	0.282309	−13.8	1389	1805
HY-18-05	112.0	60.5	12111	0.004995	0.282009	0.000014	0.014026	0.000619	0.282007	−24.6	1732	2394
HY-18-06	113.5	83.2	9054	0.009188	0.282137	0.000020	0.025315	0.001056	0.282135	−20.0	1573	2146
HY-18-07	118.2	71.9	7718	0.009320	0.282253	0.000021	0.063976	0.002588	0.282248	−16.0	1470	1924
HY-18-08	115.7	117	7855	0.014859	0.282322	0.000019	0.041118	0.001696	0.282318	−13.5	1338	1789
HY-18-11	119.2	263	9358	0.028089	0.282226	0.000019	0.051928	0.002128	0.282222	−16.9	1491	1975
HY-18-12	115.7	92.1	8663	0.010635	0.282224	0.000017	0.037552	0.001497	0.282221	−17.0	1469	1978

Table 5
Major and trace element results of apatite of Haiyang A-type granite complex sample.

Element	HY18-01	HY18-02	HY18-03	HY18-04	HY01-01	HY01-04	HY01-06	HY01-10	HY01-11
CaO	55.3	55.1	54.9	54.5	54.9	54.7	54.2	54.0	54.4
P_2O_5	42.7	42.9	43.2	42.9	42.6	42.5	41.8	42.4	41.6
SiO_2	0.20	0.15	0.18	0.13	0.30	0.54	0.52	0.54	0.47
FeO	0.07	0.07	0.14	0.16	0.02	0.04	–	0.06	0.05
MnO	0.15	0.13	0.08	0.16	0.11	0.07	0.19	0.23	0.19
MgO	0.03	0.04	0.03	–	0.02	0.02	0.04	0.07	0.01
SrO	0.01	0.01	–	0.01	–	–	0.02	0.00	0.02
F	1.83	1.61	1.67	1.79	1.92	2.00	1.87	1.77	1.95
Cl	0.29	0.40	0.31	0.22	0.61	0.66	0.63	0.73	0.63
Total	99.8	99.6	99.7	99.0	99.6	99.5	98.4	98.9	98.4
F/Cl	6.30	4.04	5.43	8.00	3.15	3.03	2.95	2.40	3.12
Rb	0.24	0.09	0.16	0.72	0.06	0.31	0.00	0.09	0.40
Sr	304	662	455	772	167	207	186	153	206
Y	445	447	504	389	408	644	731	798	497
Zr	6.70	4.69	1.03	5.88	0.37	2.96	1.36	1.17	0.74
Nb	0.06	0.03	0.05	0.04	0.01	0.10	0.00	0.00	0.00
Ba	10.3	19.4	16.3	11.6	22.4	25.1	30.2	30.7	17.0
La	860	1438	1501	834	2954	2744	3485	3273	1884
Ce	2048	3098	3331	1931	4887	5287	6238	6743	3585
Pr	242	349	397	231	382	539	594	712	382
Nd	1026	1427	1670	980	1253	2064	2108	2656	1493
Sm	170	210	246	159	152	304	302	373	218
Eu	16.7	27.6	26.6	24.3	11.6	20.2	21.7	28.1	9.86
Gd	131	154	175	111	99.4	194	202	242	148
Tb	15.6	18.0	20.8	13.3	11.0	21.8	23.5	27.2	17.3
Dy	87.5	100	112	77.3	62.8	120	127	145	91.7
Ho	16.3	17.4	19.4	12.6	12.3	22.1	24.7	27.8	17.1
Er	38.7	40.7	46.5	33.6	35.7	58.7	65.4	70.7	43.7
Tm	4.67	4.95	5.44	4.17	4.86	7.60	8.82	8.98	5.23
Yb	27.4	26.7	27.4	24.2	33.1	40.7	51.1	49.5	31.1
Lu	3.48	3.43	3.52	3.01	5.60	5.79	7.14	6.36	4.01
Hf	0.03	0.03	0.01	0.08	0.03	0.11	0.03	0.04	0.01
Ta	0.04	0.00	0.00	0.01	0.00	0.00	0.00	0.00	0.01
U	1.67	1.47	1.63	0.96	72.6	10.7	13.0	12.5	8.00
Th	8.38	7.49	8.73	3.94	61.7	78.1	93.3	85.3	31.7
Pb	4.53	3.89	4.23	3.89	2.66	3.83	3.02	3.85	2.02

ages range from 1900 to 2280 Ma, indicating addition of components from crustal or enriched mantle materials to the source. Zircon grains from the Haiyang syenite (HY-18) also have largely varied $^{176}Hf/^{177}Hf$ ratios of 0.282009 to 0.282322. The $\varepsilon_{Hf}(t)$ values range from −24.6 to −13.5 (Fig. 9), and correspondingly, their two-stage Hf model ages mainly range from 1790 to 2390 Ma.

Forty zircons from the K-feldspar granite (HY-01) and the syenite (HY-18) each have been analyzed for O isotope. The syenite zircon O isotope has larger range (4.68–9.31‰) than those of the K-feldspar granite zircons (6.65–7.78‰) and the zircon O isotope peak value of the K-feldspar granite in the frequency diagram is higher than those of the syenite, but their peak values are marginally higher than mantle zircon O isotope values (5.3 ± 0.3‰) (Valley et al., 1998) (Fig. 9).

4.4. Apatite

Thirteen apatite grains from the K-feldspar granite (HY-01) and the syenite sample (HY-18) each have been analyzed. These apatites are enriched in fluorine contents, 1.77–2.34 wt.% for HY-01 and 1.61–2.50

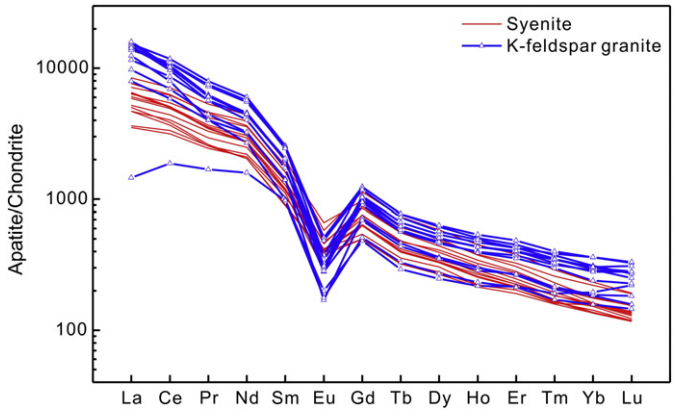

Fig. 10. Apatite chondrite-normalized REE diagram for Haiyang K-feldspar granite (HY-01) and syenite (HY-18). Chondritic values were from Sun and McDonough (1989). All REEs have a strong decline to right. Apatites of K-feldspar granite are more enriched in REEs with stronger negative Eu anomaly than those of syenite.

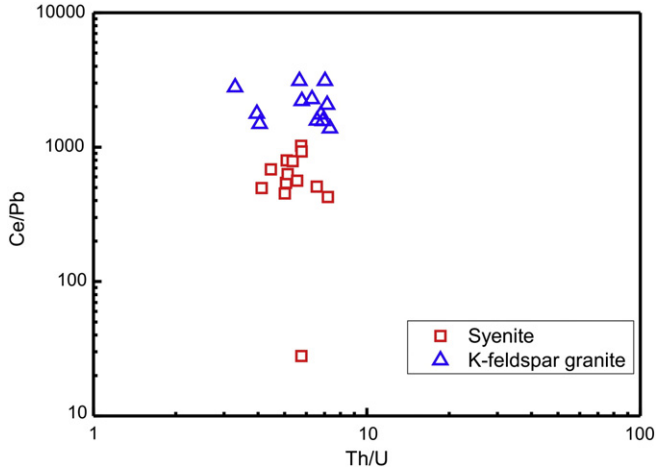

Fig. 11. Apatite Ce/Pb vs Th/U diagram, showing higher Ce/Pb ratios of Haiyang K-feldspar granite than syenite, which can be plausibly explained by more influence from subduction released fluids.

wt.% for sample HY-18 (Table 5). The apatites from the K-feldspar granite have higher chlorine contents (0.51–0.73 wt.%) than those from the syenite (0.23–0.36 wt.%). All of the apatites in these samples are enriched in LREE with a strong downward sloping pattern toward the HREE (Fig. 10). Apatites from K-feldspar granite (HY-01) are more enriched in LREE (La/Yb_N = 39.4 to 64.0) than those from syenite (HY-18) (La/Yb_N = 22.5 to 47.6). The apatite Ce/Pb ratios of K-feldspar granite (1565–3116) are markedly higher than those of syenite (28–1025) with comparable Th/U ratios (Fig. 11).

5. Discussion

5.1. Chemical characteristics of A-type granites

A-type granites, standing for alkaline, anorogenic and anhydrous, are characterized by enrichments of $K_2O + Na_2O$ and incompatible elements (e.g. REEs (except Eu), Zr, Y, Nb, Ce) and high $FeO_T/(FeO_T + MgO)$. Aluminous granites, with depleted HFSE, were plotted into VAG area in the Nb–Y and Rb–(Nb + Y) diagrams of Pearce (Bonin, 2007; Pearce et al., 1984; Whalen et al., 1987). The studied granites plot in A-type granite area in the A-type granite discrimination diagram (Fig. 12) (Frost and Frost, 2011; Frost et al., 2001). They all have high Ga/Al ratios (10,000 * Ga/Al ratio from 2.69 to 3.63). The K-feldspar granite has relatively lower $FeO_T/(FeO_T + MgO)$ ratios and the syenite is ferroan granite inclined to magnesian (Fig. 12A). Both K-feldspar granite and syenite are alkalic–calcic rocks and clearly belong to the A-type granite family (Fig. 12B).

A-type granite has been further divided into A_1 and A_2 chemical subgroups (Eby, 1992). A_1-type granites have chemical characteristics similar to those observed for oceanic-island basalts (OIB) and are thus mantle derived with intraplate settings. In contrast, A_2-type granites are similar to rocks of continental crust or island arc origins formed at convergent plate margins (Eby, 1992). Therefore, the arc signature of A_2-type granites may have been originally introduced through subduction released fluids (Li et al., 2012b).

The Haiyang syenite samples plot in the A_1 subgroup and overlap with the OIB field, compatible with an intraplate setting (Fig. 13). Although the Haiyang K-feldspar granite plots into the A_1-type granite field in Fig. 13, but it is different from the syenite and plots closer to A_2-type granite field, showing a tendency towards A_2-type. In Fig. 14, K-feldspar granite plots partially in A_2-type granite, whereas syenite samples plot near the demarcation line.

A_2-type granites have chemical composition similar to island arc basalt, which are likely influenced by the melting of metasomatized lithosphere mantle (Li et al., 2012b), with high oxygen fugacity (fO_2) (Sun et al., 2007). Although plot marginally between A_1 and A_2, the Haiyang K-feldspar granite has fO_2 even higher than A_2-type granite in the LYR belt, as indicated by zircon Ce^{4+}/Ce^{3+} in Fig. 15. The high fO_2 of A-type granites from the LYR belt has been attributed to partial melting of metasomatized lithosphere mantle (Li et al., 2012b). Analogously,

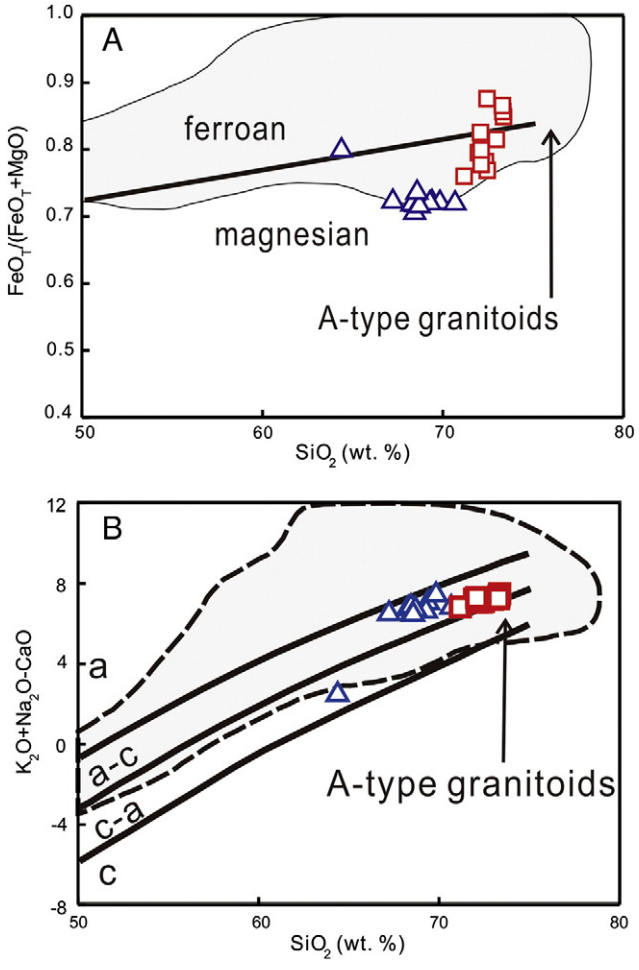

Fig. 12. A. $FeO_T/(FeO_T + MgO)$ vs SiO_2 diagram, showing all samples are A-type granites. The K-feldspar granite has relatively lower $FeO_T/(FeO_T + MgO)$ ratio and the syenite is ferroan granite inclined to magnesian; B. $K_2O + Na_2O$–CaO vs SiO_2 discrimination diagram, showing both K-feldspar granite and syenite plotted into A-type granite area and belonging to alkalic–calcic rock series. Symbols as Fig. 11.
Modified after Frost and Frost (2011) and Frost et al. (2001).

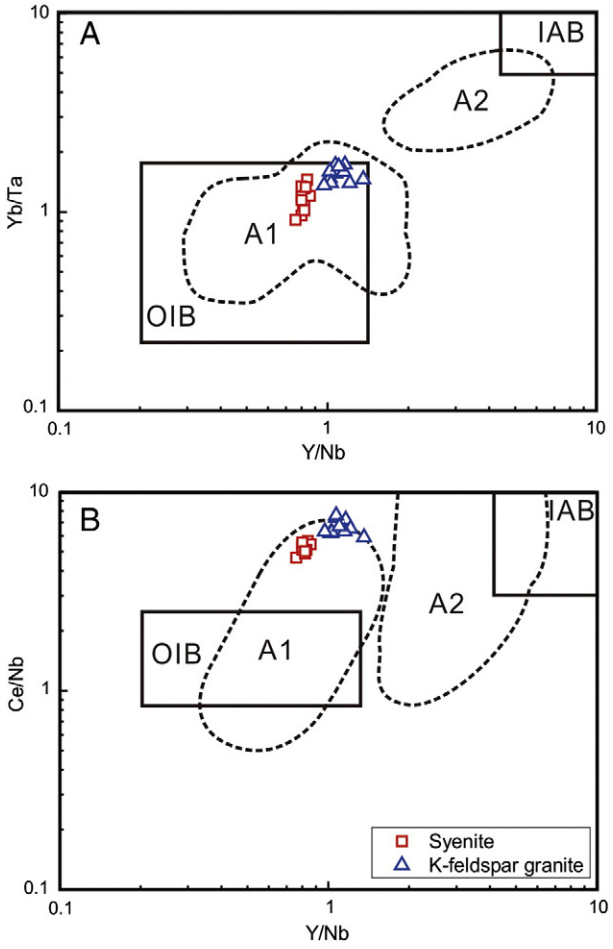

Fig. 13. A. Yb/Ta versus Y/Nb and B. Y/Nb versus Ce/Nb diagrams for the Haiyang A-type complex (Eby, 1992). OIB = oceanic island basalt; IAB = island arc basalt. Fields with dashed lines represent A_1- and A_2-type granites of Eby (1990). The K-feldspar granites were plotted close to A_2-type granite and the syenite was plotted into A_1-type granite.

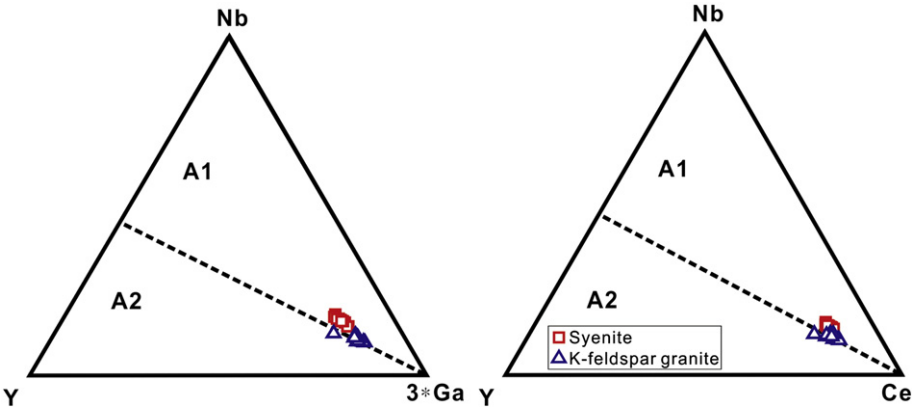

Fig. 14. Representative triangular plots for distinguishing between A_1- and A_2-type granitoids. On both diagrams, dashed line corresponds to Y/Nb ratios of 1.2 (Eby, 1992). K-feldspar granite and syenite were plotted near the line of demarcation with K-feldspar granite partial to A_2-type granite and syenite partial to A_1-type granite.

the source of the Haiyang K-feldspar granite may also have been influenced by metasomatic lithosphere mantle.

5.2. Origin of the Haiyang A-type granite complex

According to their trace element characteristics, the Haiyang K-feldspar granite and syenite are enriched in LREEs and LILEs, i.e. Rb, Sr, Ba, La and especially Pb, pointing to LILEs and LREEs enriched sources. Their trace element pattern in the primitive mantle-normalized trace element diagram is similar to the middle continental crust, and is more enriched in LILEs than lower continental crust, indicating influences from subduction released fluids and/or continental materials. The LREE enrichment of the Haiyang K-feldspar granite is more obvious than the Haiyang syenite or the A-type granites in the LYR belt (Fig. 6). In a Ce/Pb versus Nb/U diagram, the K-feldspar granites have systematically higher Ce/Pb ratios (4.05–6.95) than the syenite (1.90–4.81) with comparable Nb/U ratios (3.00–5.67) (Fig. 16). Both Ce/Pb and Nb/U rations are considerably lower than those of the mantle and MORB (Hofmann, 1997; Sun et al., 2008, 2012), but are similar to those of the continental crust (Rudnick and Gao, 2003). The Ce/Pb ratios of syenite are even lower than average continental crust (Rudnick and Gao, 2003). Given that Pb and U are more mobile than Ce and Nb, respectively, during plate subduction (McCulloch and Gamble, 1991; Pearce and Peate, 1995; Sun et al., 2008), the lower Ce/Pb ratios of syenite seemingly indicate a greater influence from subduction released fluids than K-feldspar granite (Fig. 16). This is in contrast to the lower oxygen fugacity of the syenite, implying fractionations of the different elements and oxygen fugacity above the subducting slab.

Because zircon is a very stable mineral, its trace element and isotope compositions may reflect information of the source magmas. The large variation of zircon $\varepsilon_{Hf}(t)$ values of the syenite, ranging from −24.6 to −13.5, indicates enriched sources, e.g., sediments (Woodhead et al., 2011), continental crust and/or enriched mantle components (Li et al., 2009), with/without contributions from depleted mantle, e.g., depleted portion of the lithospheric mantle (less likely) or the asthenosphere (preferred). The systematically lower zircon $\varepsilon_{Hf}(t)$ values of the K-feldspar granite than those of the syenite indicate more enriched components.

Similar to the zircon Hf isotopes, zircon O isotopes also vary dramatically, indicating at least two components. The O isotope of Haiyang complex zircons is slightly but systematically higher than those of the mantle, but far lower than sediments, indicating their source involved mantle source and slab melt, with minor sediment source (Bindeman, 2008; Li et al., 2009; Valley et al., 1998). The oxygen isotopes of K-feldspar granites have a frequency distribution peak higher than the syenite, closer to the mantle value, representing less metasomatism (Bindeman, 2008; Liu et al., 2014; Valley et al., 1998) (Fig. 9B). This is consistent with their closer affinities to A_1 granite.

Apatites from the Haiyang granite complex are also enriched in LREE, and plotted into mantle source region in the REE discrimination diagram (Fig. 17) (Zhu et al., 2004), indicating mantle components. The high F content and moderate Cl content of the apatite reflect the characteristics of host rocks, because in a granitic

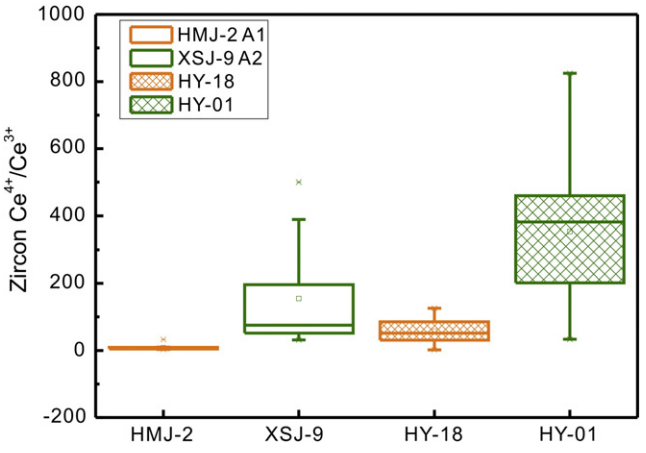

Fig. 15. The oxygen fugacities of A_1- and A_2-type granites in the Haiyang and the LYR belt indicated by zircon Ce^{4+}/Ce^{3+}. HY-01 and HY-18 represent Haiyang K-feldspar granite (A_2-type granite) and syenite (A_1-type granite); HMJ-2 and XSJ-9 represent Huangmeijian A_1-type granite and Xiangshuijian A_2-type granite in the LYR belt (Li et al., 2012b). Haiyang A_2-type granite has obviously higher fO_2 than A_2-type granite of the LYR belt, and so does the Haiyang A_1-type granite.

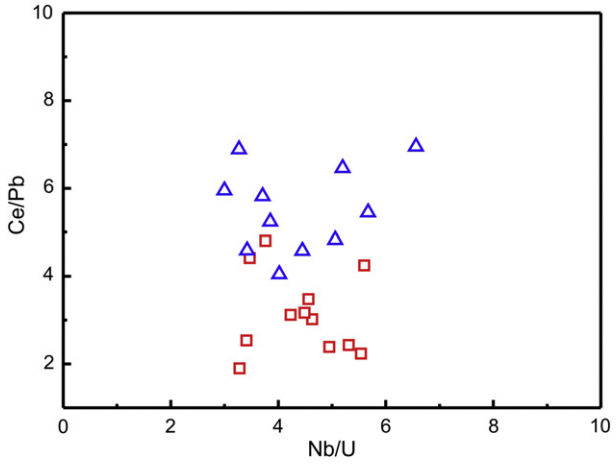

Fig. 16. Ce/Pb vs Nb/U ratio diagram, showing the K-feldspar granite having higher Ce/Pb ratio than syenite but with comparable Nb/U ratios. Symbols as Fig. 5.

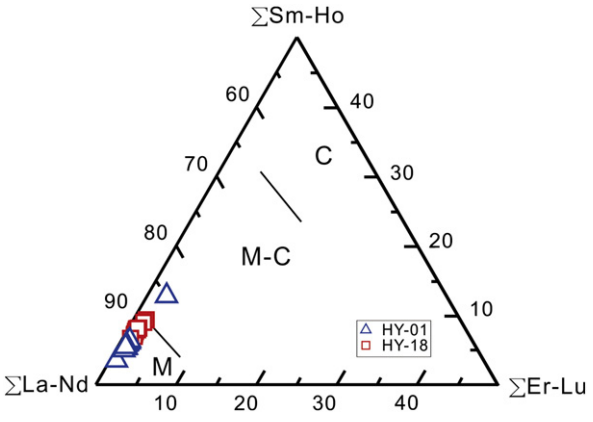

Fig. 17. ∑La ~ Nd–∑Sm ~ Ho–∑Er ~ Lu triangle diagram of the apatites, showing that Haiyang K-feldspar granite (HY-01) and syenite (HY-18) have major mantle contributions, with a little crustal addition. M stands for mantle origin; M–C stands for mixing of mantle and crust origin; and C stands for crustal origin.

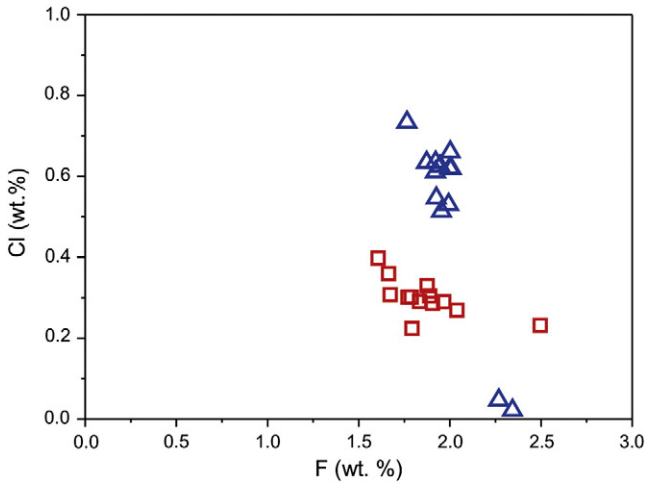

Fig. 18. Cl vs F diagram of the apatites, showing Haiyang K-feldspar granite (HY-01) and syenite (HY-18) having high F content and K-feldspar granite having higher Cl content than the syenite. Symbols as Fig. 17.

magma, the Cl concentration of the apatite is a simple linear function with the concentration of Cl in fluid, whereas the majority of fluorine in magmas goes into the crystallizing apatite (Webster et al., 2009). So the magmatic source of the Haiyang granite complex has a high F and moderately high Cl content. Fluorine is mainly retained in phengite and apatite during plate subduction, which is stable at shallow depths. For example, phengite is stable between depths of 70 and 300 km (Sorensen et al., 1997), depending on temperatures. But it can be decomposed during asthenosphere upwelling, e.g., caused by ridge subduction or slab rollback (Li et al., 2012a). In contrast to F, most of the Cl is hosted by amphibole. The higher Cl contents in the K-feldspar granite relative to the syenite indicate more contributions from the decomposition of chlorine mineral, such as amphibole. Amphibole is apt to decomposition and release Cl into the fluids (Volfinger et al., 1985; Zhang et al., 2012). Melting of the source which has been metasomated by Cl-enriched fluid may result in high Cl content magma. Therefore, higher Cl content in Haiyang K-feldspar granite than syenite may reflect that the K-feldspar granite is derived from a source with more contributions from subduction released fluids (Fig. 18). This is again consistent with most other geochemical characteristics discussed above.

5.3. Petrogenesis of the Haiyang A-type granite complex

The Haiyang A-type granite complex plots mainly in the A_1 subgroup. Detailed geochemical characteristics, however, show a tendency of transition originally from A_2 to A_1 subgroups. This can be plausibly interpreted by partial melting of a slightly metasomatized mantle domain. Mantle components metasomatized by subduction released fluids are easier to be partially melted, therefore K-feldspar granite (A_2 type) with higher oxygen fugacity may be formed slightly earlier, which eliminated subducted signatures, and then A_1 type syenite was formed.

Previous study on A-type granites in the LYR belt shows that A_1 and A_2 subgroup granites have nearly the same age and are closely associated with each other (Li et al., 2012b). These two types of A-type granite in the LYR belt were interpreted as induced by ridge subduction (Li et al., 2012b). The Haiyang K-feldspar granites have nearly the same geochemical characteristics as the A_2-type granite in the LYR belt, with high fO_2 and addition of subduction material. Also an adakite belt of slightly older ages has been reported in the Xuhuai and Shandong region next to the A-type granite belt (Ling et al., 2013), i.e., the rock association of Shandong Peninsula is similar with the LYR belt. Thus, the petrogenesis of Haiyang A-type granite complex can best be explained by a ridge subduction model. Given that the age of the Haiyang A-type granite complex is close to the peak of the destruction of the North China Craton, our results support previous proposed model that the ridge subduction along the Shandong Peninsula is also the important mechanism inducing the decratonization of the NCC (Ling et al., 2013).

6. Conclusion

Geochemical data indicate that the Haiyang K-feldspar granite and syenite are typical A-type granites and are characterized by high Fe * (FeO_T/(FeO_T + MgO)) and 10,000 * Ga/Al ratios, total alkali and enrichments of LILE. Zircon U–Pb ages of the Haiyang K-feldspar granite and syenite are 116.8 ± 1.7 Ma and 115.8 ± 2.2 Ma, respectively. Large variation of the $\varepsilon_{Hf}(t)$ values of the K-feldspar granite (−22.4 to −15.6) and the syenite (−24.6 to −13.5), together with varied O isotopes, indicates highly varied sources. Peak values of zircon O isotope marginally higher than mantle source zircon reflect mantle contributions to the Haiyang A-type granite. The enrichment of LREE in apatites shows more influence of subduction fluids on K-feldspar granite, which is supported by higher Cl content in its apatite.

The Haiyang complex contains rocks identifiable with both A_1 and A_2 chemical subgroups. The K-feldspar granite plots near the boundary between the A_1 and A_2-type granites and crystallized under higher oxygen fugacity conditions as indicated by zircon Ce^{4+}/Ce^{3+} ratios, and the syenite lies more within the field of A_1-type granite and crystallized under a lower oxygen fugacity. This petrogenetic history of the massif can plausibly be interpreted with a ridge subduction model, which also served as the trigger mechanism for the decratonization of the North China Craton.

Acknowledgments

The study is supported by National Natural Science Foundation of China (Nos. 41090374, 41121002). The authors would like to thank two anonymous referees for constructive review comments and editor Dr. Nelson Eby for constructive suggestions. GIG contribution No. 1890.

References

Ballard, J.R., Palin, J.M., Campbell, I.H., 2002. Relative oxidation states of magmas inferred from Ce(IV)/Ce(III) in zircon: application to porphyry copper deposits of northern Chile. Contributions to Mineralogy and Petrology 144, 347–364.

Belousova, E.A., Griffin, W.L., Suzanne, Y.O.R., Fisher, N.I., 2002. Igneous zircon: trace element composition as an indicator of source rock type. Contributions to Mineralogy and Petrology 143, 602–622.

Bindeman, I., 2008. Oxygen isotopes in mantle and crustal magmas as revealed by single crystal analysis. Reviews in Mineralogy and Geochemistry 69, 445–478.

BlichertToft, J., Chauvel, C., Albarede, F., 1997. Separation of Hf and Lu for high-precision isotope analysis of rock samples by magnetic sector multiple collector ICP-MS. Contributions to Mineralogy and Petrology 127, 248–260.
Bonin, B., 2007. A-type granites and related rocks: evolution of a concept, problems and prospects. Lithos 97, 1–29.
Chen, L., 2010. Concordant structural variations from the surface to the base of the upper mantle in the North China Craton and its tectonic implications. Lithos 120, 96–115.
Chu, N.C., Taylor, R.N., Chavagnac, V., Nesbitt, R.W., Boella, R.M., Milton, J.A., German, C.R., Bayon, G., Burton, K., 2002. Hf isotope ratio analysis using multi-collector inductively coupled plasma mass spectrometry: an evaluation of isobaric interference corrections. Journal of Analytical Atomic Spectrometry 17, 1567–1574.
De Biévre, P., Taylor, P.D.P., 1993. Table of the isotopic compositions of the elements. International Journal of Mass Spectrometry and Ion Processes 123, 149–166.
Eby, G.N., 1990. The A-type granitoids a review of their occurrence and chemical characteristics and speculations their petrogenesis. Lithos 26, 115–134.
Eby, G.N., 1992. Chemical subdivision of the A-typy granitoids petrogenetic and tectonic implications. Geology 20, 641–644.
Fan, W.M., Guo, F., Wang, Y.J., Lin, G., Zhang, M., 2001. Post-orogenic bimodal volcanism along the Sulu orogenic belt in eastern China. Physics and Chemistry of the Earth, Part A: Solid Earth and Geodesy 26, 733–746.
Frost, C.D., Frost, B.R., 2011. On ferroan (A-type) granitoids: their compositional variability and modes of origin. Journal of Petrology 52, 39–53.
Frost, B.R., Barnes, C.G., Collins, W.J., Arculus, R.J., Ellis, D.J., Frost, C.D., 2001. A geochemical classification for granitic rocks. Journal of Petrology 42, 2033–2048.
Gao, S., Rudnick, R.L., Yuan, H.L., Liu, X.M., Liu, Y.S., Xu, W.L., Ling, W.L., Ayers, J., Wang, X.C., Wang, Q.H., 2004. Recycling lower continental crust in the North China craton. Nature 432, 892–897.
Goss, S.C., Wilde, S.A., Wu, F., Yang, J., 2010. The age, isotopic signature and significance of the youngest Mesozoic granitoids in the Jiaodong Terrane, Shandong Province, North China Craton. Lithos 120, 309–326.
Green, T.H., Pearson, N.J., 1986. Ti-rich accessory phase saturation in hydrous mafic–felsic compositions at high P, T. Chemical Geology 54, 185–201.
Griffin, W.L., Pearson, N.J., Belousova, E., Jackson, S.E., van Achterbergh, E., O'Reilly, S.Y., Shee, S.R., 2000. The Hf isotope composition of cratonic mantle: LAM-MC-ICPMS analysis of zircon megacrysts in kimberlites. Geochimica et Cosmochimica Acta 64, 133–147.
Griffin, W.L., Wang, X., Jackson, S.E., Pearson, N.J., O'Reilly, S.Y., Xu, X.S., Zhou, X.M., 2002. Zircon chemistry and magma mixing, SE China: in-situ analysis of Hf isotopes, Tonglu and Pingtan igneous complexes. Lithos 61, 237–269.
Harrison, T.M., Watson, E.B., 1984. The behavior of apatite during crustal anatexis—equilibrium and kinetic considerations. Geochimica et Cosmochimica Acta 48, 1467–1477.
Hofmann, A.W., 1997. Mantle geochemistry: the message from oceanic volcanism. Nature 385, 219–229.
Hoskin, P.W.O., Black, L.P., 2000. Metamorphic zircon formation by solid-state recystallization of protolith igneous zircon. Journal of Metamorphic Geology 18, 423–439.
Ickert, R., Hiess, J., Williams, I., Holden, P., Ireland, T., Lanc, P., Schram, N., Foster, J., Clement, S., 2008. Determining high precision, in situ, oxygen isotope ratios with a SHRIMP II: analyses of MPI-DING silicate-glass reference materials and zircon from contrasting granites. Chemical Geology 257, 114–128.
Li, S.G., Xiao, Y.L., Liou, D.L., Chen, Y.Z., Ge, N.J., Zhang, Z.Q., Sun, S.S., Cong, B.L., Zhang, R.Y., Hart, S.R., Wang, S.S., 1993. Collision of the North China and Yangtse blocks and formation of coesite-bearing eclogites; timing and processes. Chemical Geology 109, 89–111.
Li, X.H., Qi, C.S., Liu, Y., Liang, X.R., Tu, X.L., Xie, L.W., Yang, Y.H., 2005. Petrogenesis of the Neoproterozoic bimodal volcanic rocks along the western margin of the Yangtze Block: new constraints from Hf isotopes and Fe/Mn ratios. Chinese Science Bulletin 50, 2481–2486.
Li, X., Li, W., Wang, X., Li, Q., Liu, Y., Tang, G., 2009. Role of mantle-derived magma in genesis of early Yanshanian granites in the Nanling Range, South China: in situ zircon Hf–O isotopic constraints. Science in China Series D-Earth Sciences 52, 1262–1278.
Li, C.-Y., Zhang, H., Wang, F.-Y., Liu, J.-Q., Sun, Y.-L., Hao, X.-L., Li, Y.-L., Sun, W., 2012a. The formation of the Dabaoshan porphyry molybdenum deposit induced by slab rollback. Lithos 150, 101–110.
Li, H., Ling, M.-X., Li, C.-Y., Zhang, H., Ding, X., Yang, X.-Y., Fan, W.-M., Li, Y.-L., Sun, W.-D., 2012b. A-type granite belts of two chemical subgroups in central eastern China: indication of ridge subduction. Lithos 150, 26–36.
Liang, H.Y., Campbell, I.H., Allen, C., Sun, W.D., Liu, C.Q., Yu, H.X., Xie, Y.W., Zhang, Y.Q., 2006. Zircon Ce^{4+}/Ce^{3+} ratios and ages for Yulong ore-bearing porphyries in eastern Tibet. Mineralium Deposita 41, 152–159.
Liang, J.L., Ding, X., Sun, X.M., Zhang, Z.M., Zhang, H., Sun, W.D., 2009. Nb/Ta fractionation observed in eclogites from the Chinese Continental Scientific Drilling Project. Chemical Geology 268, 27–40.
Ling, M.X., Wang, F.Y., Ding, X., Hu, Y.H., Zhou, J.B., Zartman, R.E., Yang, X.Y., Sun, W.D., 2009. Cretaceous ridge subduction along the lower Yangtze River Belt, eastern China. Economic Geology 104, 303–321.
Ling, M.-X., Li, Y., Ding, X., Teng, F.-Z., Yang, X.-Y., Fan, W.-M., Xu, Y.-G., Sun, W., 2013. Destruction of the North China craton induced by ridge subductions. Journal of Geology 121, 197–213.
Liu, D.Y., Nutman, A.P., Compston, W., Wu, J.S., Shen, Q.H., 1992. Remnants of ≥3800 Ma crust in the Chinese part of the Sino-Korean craton. Geology 20, 33342.
Liu, Y.S., Hu, Z.C., Gao, S., Gunther, D., Xu, J., Gao, C.G., Chen, H.H., 2008. In situ analysis of major and trace elements of anhydrous minerals by LA-ICP-MS without applying an internal standard. Chemical Geology 257, 34–43.
Liu, Y.S., Gao, S., Hu, Z.C., Gao, C.G., Zong, K.Q., Wang, D.B., 2010. Continental and oceanic crust recycling-induced melt–peridotite interactions in the Trans-North China Orogen: U–Pb dating, Hf isotopes and trace elements in zircons from mantle xenoliths. Journal of Petrology 51, 537–571.
Liu, C.-Z., Wu, F.-Y., Chung, S.-L., Li, Q.-L., Sun, W.-D., Ji, W.-Q., 2014. A 'hidden' ^{18}O-enriched reservoir in the sub-arc mantle. Scientific Reports 4.
Loiselle, M.C., Wones, D.R., 1979. Characteristics of anorogenic granites. Geological Society of America Abstracts with Programs 11, 468.
McCulloch, M.T., Gamble, J.A., 1991. Geochemical and geodynamical constraints on subduction zone magmatism. Earth and Planetary Science Letters 102, 358–374.
Pearce, J.A., Peate, D.W., 1995. Tectonic implications of the composition of volcanic arc magmas. Annual Review of Earth and Planetary Sciences 23, 251–285.
Pearce, J.A., Harris, N.B.W., Tindle, A.G., 1984. Trace element discrimination diagrams for the tectonic interpretation of granitic rocks. Journal of Petrology 25, 956–983.
Rudnick, R.L., Gao, S., 2003. Composition of the continental crust. In: Rudnick, R.L. (Ed.), Treatise on Geochemistry. Elsevier, pp. 1–64.
Soderlund, U., Patchett, J.P., Vervoort, J.D., Isachsen, C.E., 2004. The Lu-176 decay constant determined by Lu–Hf and U–Pb isotope systematics of Precambrian mafic intrusions. Earth and Planetary Science Letters 219, 311–324.
Sorensen, S.S., Grossman, J.N., Perfit, M.R., 1997. Phengite-hosted LILE enrichment in eclogite and related rocks: implications for fluid-mediated mass transfer in subduction zones and arc magma genesis. Journal of Petrology 38, 3–34.
Sun, S.S., McDonough, W.F., 1989. Chemical and isotopic systematics of oceanic basalts: implications for mantle composition and processed. Magmatism in the Ocean Basins. Geological Society Special Publication, 42, pp. 313–345.
Sun, W.D., Williams, I.S., Li, S.G., 2002. Carboniferous and Triassic eclogites in the western Dabie Mountains, east-central China: evidence for protracted convergence of the North and South China blocks. Journal of Metamorphic Geology 20, 873–886.
Sun, X.M., Tang, Q., Sun, W.D., Xu, L., Zhai, W., Liang, J.L., Liang, Y.H., Shen, K., Zhang, Z.M., Zhou, B., Wang, F.Y., 2007. Monazite, iron oxide and barite exsolutions in apatite aggregates from CCSD drillhole eclogites and their geological implications. Geochimica et Cosmochimica Acta 71, 2896–2905.
Sun, W.D., Hu, Y.H., Kamenetsky, V.S., Eggins, S.M., Chen, M., Arculus, R.J., 2008. Constancy of Nb/U in the mantle revisited. Geochimica et Cosmochimica Acta 72, 3542–3549.
Sun, W.D., Ling, M.X., Yang, X.Y., Fan, W.M., Ding, X., Liang, H.Y., 2010. Ridge subduction and porphyry copper–gold mineralization: an overview. Science China Earth Sciences 53, 475–484.
Sun, W.D., Ling, M.X., Chung, S.L., Ding, X., Yang, X.Y., Liang, H.Y., Fan, W.M., Goldfarb, R., Yin, Q.Z., 2012. Geochemical constraints on adakites of different origins and copper mineralization. Journal of Geology 120, 105–120.
Tan, J., Wei, J., Audétat, A., Pettke, T., 2012. Source of metals in the Guocheng gold deposit, Jiaodong Peninsula, North China Craton: link to early Cretaceous mafic magmatism originating from Paleoproterozoic metasomatized lithospheric mantle. Ore Geology Reviews 48, 70–87.
Trotter, J.A., Williams, I.S., Barnes, C.R., Lecuyer, C., Nicoll, R.S., 2008. Did cooling oceans trigger ordovician biodiversification? Evidence from conodont thermometry. Science 321, 550–554.
Tu, X.L., Zhang, H.F., Deng, W.F., Liang, H.Y., Sun, W.D., 2011. Application of resolution laser ablation ICPMS in trace element analyses. Geochimica 40, 83–98 (in Chinese with English abstract).
Valley, J.W., Kinny, P.D., Schulze, D.J., Spicuzza, M.J., 1998. Zircon megacrysts from kimberlite: oxygen isotope variability among mantle melts. Contributions to Mineralogy and Petrology 133, 1–11.
Volfinger, M., Robert, J.L., Vielzeuf, D., Neiva, A.M.R., 1985. Structural control of the chlorine content of OH-bearing silicates (micas and amphiboles). Geochimica et Cosmochimica Acta 49, 37–48.
Wang, D.Z., Zhao, G.T., Qiu, J.S., 1995. The tectonic constraint on the late mesozoic A-type granitoids in eastern China. Geological Journal of China Universities 1, 13–21.
Wang, T., Liu, S., Hu, R.Z., Feng, C.X., Qi, Y.Q., Feng, G.Y., Wang, C.H., 2009. Elemental geochemistry and petrogenesis of A-type granites in the Sulu orogen. Journal of Jilin University (Earth Science Edition) 39, 676–688.
Webster, J.D., Tappen, C.M., Mandeville, C.W., 2009. Partitioning behavior of chlorine and fluorine in the system apatite–melt–fluid. II: felsic silicate systems at 200 MPa. Geochimica et Cosmochimica Acta 73, 559–581.
Whalen, J.B., Currie, K.L., Chappell, B.W., 1987. A-type granites geochemical characteristics, discrimination and petrogenesis. Contributions to Mineralogy and Petrology 95, 407–419.
Woodhead, J., Hergt, J., Shelley, M., Eggins, S., Kemp, R., 2004. Zircon Hf-isotope analysis with an excimer laser, depth profiling, ablation of complex geometries, and concomitant age estimation. Chemical Geology 209, 121–135.
Woodhead, J., Hergt, J., Greig, A., Edwards, L., 2011. Subduction zone Hf-anomalies: mantle messenger, melting artefact or crustal process? Earth and Planetary Science Letters 304, 231–239.
Wu, F.-Y., Walker, R.J., Yang, Y.-H., Yuan, H.-L., Yang, J.-H., 2006. The chemical–temporal evolution of lithospheric mantle underlying the North China Craton. Geochimica et Cosmochimica Acta 70, 5013–5034.
Xu, Y.G., 2001. Thermo-tectonic destruction of the archaean lithospheric keel beneath the Sino-Korean Craton in China: evidence, timing and mechanism. Physics and Chemistry of the Earth, Part A: Solid Earth and Geodesy 26, 747–757.
Xu, Y.G., 2006. Using basalt geochemistry to constrain Mesozoic–Cenozoic evolution of the lithosphere beneath North China Craton. Earth Science Frontiers 13, 93–104 (in Chinese with English abstract).
Xu, Y.G., Huang, X.L., Ma, J.L., Wang, Y.B., Iizuka, Y., Xu, J.F., Wang, Q., Wu, X.Y., 2004. Crust–mantle interaction during the tectono-thermal reactivation of the North China Craton: constraints from SHRIMP zircon U–Pb chronology and geochemistry

of Mesozoic plutons from western Shandong. Contributions to Mineralogy and Petrology 147, 750–767.
Xu, Y.G., Zhang, H.H., Qiu, H.N., Ge, W.C., Wu, F.Y., 2012. Oceanic crust components in continental basalts from Shuangliao, Northeast China: derived from the mantle transition zone? Chemical Geology 328, 168–184.
Yang, J.H., Wu, F.Y., Wilde, S.A., 2003. A review of the geodynamic setting of large-scale Late Mesozoic gold mineralization in the North China Craton: an association with lithospheric thinning. Ore Geology Reviews 23, 125–152.
Yang, J.-H., Wu, F.-Y., Chung, S.-L., Wilde, S.A., Chu, M.-F., Lo, C.-H., Song, B., 2005. Petrogenesis of Early Cretaceous intrusions in the Sulu ultrahigh-pressure orogenic belt, east China and their relationship to lithospheric thinning. Chemical Geology 222, 200–231.
Ying, J.F., Zhou, X.H., Zhang, H.F., 2006. The geochemical variations of mid-Cretaceous lavas across western Shandong Province, China and their tectonic implications. International Journal of Earth Sciences 95, 68–79.
Yuan, H.L., Gao, S., Dai, M.N., Zong, C.L., Gunther, D., Fontaine, G.H., Liu, X.M., Diwu, C., 2008. Simultaneous determinations of U–Pb age, Hf isotopes and trace element compositions of zircon by excimer laser-ablation quadrupole and multiple-collector ICP-MS. Chemical Geology 247, 100–118.
Zhang, H.-F., 2012. Destruction of ancient lower crust through magma underplating beneath Jiaodong Peninsula, North China Craton: U–Pb and Hf isotopic evidence from granulite xenoliths. Gondwana Research 21, 281–292.
Zhang, H.F., Sun, M., 2002. Geochemistry of mesozoic basalts and mafic dikes, southeastern North China craton, and tectonic implications. International Geology Review 44, 370–382.
Zhang, Q., Wang, Y., Qian, Q., Yang, J.H., Wang, Y.L., Zhao, T.P., Guo, G.J., 2001. The characteristics and tectonic–metallogenic significances of the adakites in Yanshan period from eastern China. Acta Petrologica Sinica 17, 236–244 (in Chinese with English abstract).
Zhang, H.F., Sun, M., Zhou, X.H., Fan, W.M., Zhai, M.G., Yin, J.F., 2002. Mesozoic lithosphere destruction beneath the North China Craton: evidence from major-, trace-element and Sr–Nd–Pb isotope studies of Fangcheng basalts. Contributions to Mineralogy and Petrology 144, 241–253.
Zhang, J., Zhao, Z.F., Zheng, Y.F., Dai, M.N., 2010. Postcollisional magmatism: geochemical constraints on the petrogenesis of Mesozoic granitoids in the Sulu orogen, China. Lithos 119, 512–536.
Zhang, C., Holtz, F., Ma, C., Wolff, P., Li, X., 2012. Tracing the evolution and distribution of F and Cl in plutonic systems from volatile-bearing minerals: a case study from the Liujiawa pluton (Dabie orogen, China). Contributions to Mineralogy and Petrology 164, 859–879.
Zhao, L., Zheng, T.Y., Lu, G., 2013. Distinct upper mantle deformation of cratons in response to subduction: constraints from SKS wave splitting measurements in eastern China. Gondwana Research 23, 39–53.
Zheng, Y.-F., Wu, Y.-B., Zhao, Z.-F., Zhang, S.-B., Xu, P., Wu, F.-Y., 2005. Metamorphic effect on zircon Lu–Hf and U–Pb isotope systems in ultrahigh-pressure eclogite-facies metagranite and metabasite. Earth and Planetary Science Letters 240, 378–400.
Zheng, Y.-F., Zhao, Z.-F., Wu, Y.-B., Zhang, S.-B., Liu, X., Wu, F.-Y., 2006. Zircon U–Pb age, Hf and O isotope constraints on protolith origin of ultrahigh-pressure eclogite and gneiss in the Dabie orogen. Chemical Geology 231, 135–158.
Zhu, X.Q., Wang, Z.G., Huang, Y., Wang, H.L., 2004. REE content and distribution in apatite and its geological tracing significance. Chinese Rare Earths 25, 41.
Zhu, R.-X., Yang, J.-H., Wu, F.-Y., 2012. Timing of destruction of the North China Craton. Lithos 149, 51–60.